

7-12-2014

# Design, Fabrication, and Characterization of a MEMS Based Thermally Actuated Fabry-Pérot Interferometer.

Andrew Ian Young

Follow this and additional works at: [https://digitalrepository.unm.edu/me\\_etds](https://digitalrepository.unm.edu/me_etds)

---

## Recommended Citation

Young, Andrew Ian. "Design, Fabrication, and Characterization of a MEMS Based Thermally Actuated Fabry-Pérot Interferometer." (2014). [https://digitalrepository.unm.edu/me\\_etds/83](https://digitalrepository.unm.edu/me_etds/83)

This Thesis is brought to you for free and open access by the Engineering ETDs at UNM Digital Repository. It has been accepted for inclusion in Mechanical Engineering ETDs by an authorized administrator of UNM Digital Repository. For more information, please contact [disc@unm.edu](mailto:disc@unm.edu).

Andrew Ian Young

*Candidate*

---

Mechanical Engineering

*Department*

---

This thesis is approved, and it is acceptable in quality and form for publication:

*Approved by the Thesis Committee:*

Dr. Zayd C. Leseman, Chairperson

---

Dr. Yu-Lin Shen

---

Dr. Gregory N. Nielson

---

---

---

---

---

---

---

---

---

**DESIGN, FABRICATION, AND CHARACTERIZATION OF A  
MEMS BASED THERMALLY ACTUATED FABRY-PÉROT  
INTERFEROMETER**

**by**

**ANDREW IAN YOUNG**

**B.S.M.E UNIVERSITY OF NEW MEXICO, 2009**

THESIS

Submitted in Partial Fulfillment of the  
Requirements for the Degree of

**Master of Science in  
Mechanical Engineering**

The University of New Mexico  
Albuquerque, New Mexico

**May, 2014**

## **DEDICATION**

I would like to dedicate this thesis to all of my family and friends who have supported and encouraged me while I completed this work.

## ACKNOWLEDGEMENTS

The work presented in this thesis would not have been possible to complete without the aid of various individuals at UNM and Sandia National Laboratories. First and foremost I would like to express my gratitude to my advisor Dr. Zayd C. Leseman for allowing me the opportunity to work with his research group at UNM, for being patient with me as I completed the work shown in this thesis, and for the opportunities that have resulted from working on this project.

I am also deeply indebted to my colleague Dr. Drew Goettler for helping me with the extensive SEM and FIB work that was vital to the success of the work presented here. I would also like to thank my colleague Dr. Khawar Abbas for his help with fabricating the MEMS device, the coated fiber mirror, as well as his help with obtaining displacement results from the SEM data. I would also like to thank Francisco Benito for aiding in the design of the thermal actuators. Finally, I would like to acknowledge Dylan Wood for helping me with a bulk of the fabrication of the thermal actuators.

The devices in this thesis were fabricated at the cleanroom facilities at UNM's MTTC complex. Harold O. Madison at MTTC helped solve several fabrication issues that I encountered during the fabrication process.

David Woods and Jason Church in the UNM Mechanical Engineering Machine Shop helped fabricate the holder that allowed me to move the device from one lab to another and helped with various unrelated projects during my time at UNM.

Testing the Fabry-Pérot cavity would not have been possible without the aid of several individuals at Sandia National Laboratories. I would like to thank Dr. Peter Rakich, Dr. Alex Robinson, Dr. Ryan Camacho, Dr. Eric Langlois, Dr. Greg Nelson, Mike Baker,

Michael J Shaw, and Victor Yarberry as well as Dr. Patrick Chu and Dr. Keith Ortiz for the opportunity to work with all of them. The multitude of skills I learned while working on various projects directly contributed to me finishing this thesis and has been the opportunity of a lifetime. Finally I would like to thank all of the people mentioned above as well as the other interns out at SNL for their conversations, advice, and friendly banter.

# **Design, Fabrication, and Characterization of a MEMS Based Thermally Actuated Fabry-Pérot Interferometer**

by

**Andrew Ian Young**

**B.S.M.E University of New Mexico, 2009**

**M.S.M.E University of New Mexico, 2014**

## **ABSTRACT**

MEMS devices have become ubiquitous in consumer devices and are also being used to conduct experiments on the nano and micro scale. There is a growing need to test the properties of materials at the micro and nanoscale. In order to test those materials, a reliable method of sensing displacement is needed. Another growing area of MEMS research is in creating micro optical cavities that allow for manipulation and control of atoms in QED research. This thesis describes a MEMS based thermally actuated Fabry-Pérot cavity interferometer that has potential as a displacement sensing mechanism for use in material testers and other devices which require motion feedback. Additionally the device has a potential application as a tunable cavity for use in cavity QED experiments. The theory behind the operation of the thermal actuator and the Fabry-Pérot cavity are shown. The design of the actuator and cavity is also discussed in detail as well as the fabrication of both structures. Experiments of the device were performed in a vacuum and in air. The data obtained from experiments are compared to FEA and MATLAB simulations to verify the performance of the device.

# Table of Contents

Table of Figures .....	ix
Chapter 1: Introduction .....	1
1.1 Background and Motivation .....	1
1.1.1 Background .....	1
1.1.2 Motivation .....	1
1.2 Objective .....	3
1.3 Organization of the Document .....	4
Chapter 2: Theory of Thermal Actuators and Fabry-Pérot Cavities .....	5
2.1 Theory of the Operation of Thermal Actuators .....	5
2.1.1 Design Parameters of a Chevron Thermal Actuator .....	8
2.1.2 Analytical Models of Thermal Actuators .....	9
2.1.2.1 Heat Transfer Models Found in Literature .....	9
2.1.2.1.1 Heat Transfer Balance in a Thermal Actuator .....	10
2.1.2.1.1.1 Common Descriptions of Internal Heat Flux .....	11
2.1.2.1.1.2 Common Descriptions of Heat Conduction Within a Actuator .....	12
2.1.2.1.1.3 Heat Transfer to the Air From the Actuator in Atmospheric Tests .....	13
2.1.2.1.1.4 Common Descriptions of Radiative Heat Transfer to the Surroundings .....	16
2.1.2.1.2 Methods of Obtaining a Temperature Profile of the Actuator .....	17
2.1.2.1.2.1 Finite Difference Method of Obtaining a Temperature Profile .....	17
2.1.2.1.2.2 Explicit Forms of the Temperature Distribution .....	18
2.1.2.2 Various Analytical Mechanical Models of Thermal Actuators .....	22
2.1.2.2.1 Purely Geometrical Models .....	23
2.1.2.2.2 Beam Deformation Models .....	25
2.1.2.3 Final Remarks on Theory of Thermal Actuators .....	30
2.2 Theory of the Fabry-Pérot Cavity .....	30
2.3 Closing Remarks .....	36
Chapter 3: Design of the Thermal Actuator and the Fiber Based Fabry-Pérot Cavity .....	37
3.1 Introduction .....	37
3.2 Design of the Thermal Actuator .....	37
3.3 Design of the Fiber Based Fabry-Pérot Cavity .....	41
3.4 Concluding Remarks .....	44
Chapter 4: Fabrication of the Thermal Actuator and Fabry-Pérot Cavity .....	46
4.1 Fabrication of the Thermal Actuator .....	46
4.1.1 Fabrication of the Alignment Forks .....	48
4.1.2 Fabrication of the Trenches .....	49
4.1.3 Releasing the Structure from the Sacrificial Oxide .....	52
4.2 Description of the Chip Holder .....	54
4.3 Fabrication of the Fiber Mirror .....	55
4.4 Placement of the Fiber Mirrors onto the Thermal Actuator .....	57
4.4.1 Placement of Gold Coated Fiber Mirror onto the Shuttle .....	57
4.4.2 Placement of the Input/Output Fiber onto the Backbone Structure .....	59
Chapter 5: Experimental Setups and Testing Procedures .....	62
5.1 In-situ Testing of the Device in SEM .....	62
5.2 Testing the Fiber Based Fabry-Pérot Cavity in Air .....	66
Chapter 6: Modeling the Thermal Actuator and Fabry-Pérot Cavity .....	70
6.1 Multiphysics FEA Modeling of the Thermal Actuator in Vacuum .....	70
6.1.1 Basic Conditions and Boundaries of the FEA Model .....	71
6.1.2 Temperature Dependent Materials Used in the FEA Model .....	72



6.1.3 Results of the FEA Simulation .....	73
6.2 MATLAB Fitting of the Fiber Based Fabry-Pérot Cavity Data .....	77
6.2.1 Two-Fringe Method of Obtaining Displacement of the Actuator .....	77
6.2.2 Least-Squares Curve Fit to Determine Displacement of the Actuator .....	79
6.2.2.1 Procedure of Obtaining a Least-Squares Curve Fit to Data .....	81
6.3 Concluding Statements .....	83
Chapter 7: Results and Discussion .....	85
7.1 Tests Performed on the Thermal Actuator in SEM in Vacuum.....	85
7.2 Tests Performed on the Thermal Actuator in Air .....	87
7.3 Future Improvements to Device and Experiment .....	89
7.4 Concluding Remarks .....	92
Chapter 8: Conclusion .....	93
Appendix 1: Derivation of the Cavity Length Formula Used in the Two-Fringe Method.....	95
Appendix 2: Definition of Variables .....	97
References.....	101

## Table of Figures

Figure 1: Depiction of the Operation of a Bimorph Actuator. ....	6
Figure 2: Depiction of the Operation of a Pseudo-Bimorph Actuator.....	6
Figure 3: Depiction of the Operation of a Chevron Thermal Actuator (TA). ....	7
Figure 4: Diagram Representing Modes of Heat Transfer in a Volume Element in a TA. ....	10
Figure 5: Model of the Kinetics of a Thermal Actuator. ....	23
Figure 6: Mechanical Constraints & Free-Body Diagram Relating to Work by Zhu et al.....	26
Figure 7: Mechanical Constraints & Free-Body Diagram Relating to Work by Que et al. ....	27
Figure 8: Mechanical Constraints & Free-Body Diagram Relating to Work by Enikov et al.....	28
Figure 9: Ray Optics Approach to Deriving the Equations for A Fabry-Perot Cavity.....	32
Figure 10: Graph of the Reflected Airy Function for Different Values of Reflectivity (R).....	35
Figure 11: Isotropic Depiction of the Thermal Actuator. ....	38
Figure 12: Depiction of the Fiber Mirror Placed in the Trench on the Shuttle. ....	39
Figure 13: Depiction of TA Parameters.....	40
Figure 14: Images of Different Thermal Actuator Designs that are Fabricated. ....	40
Figure 15: Depiction of the Fabry-Pérot Cavity. ....	42
Figure 16: Reflectivity of the Fiber Mirror as a Function of the Wavelength of Incident Light....	43
Figure 17: Variation of Optical Properties with Respect to Au Film Thickness.....	44
Figure 18: Processing Steps for Fabricating Thermal Actuators.....	47
Figure 19: Image of Alignment Forks Patterned in Photoresist (PR).....	49
Figure 20: Image of Completed Alignment Marks.....	50
Figure 21: Image of Trench Patterned in Photoresist. ....	50
Figure 22: Image of a Trench from a Sectioned Scout Wafer. ....	52
Figure 23: Image of a Thermal Actuator Patterned in Photoresist. ....	53
Figure 24: SEM Image of Released Thermal Actuator. ....	53
Figure 25: A Depiction of the Chip Holder. ....	54
Figure 26: SEM Image of an Aluminum Wire Bond on a Silicon Bond Pad.....	55
Figure 27: Depiction of Bundled and Cleaved Fibers in Preparation for Coating the Fibers. ....	56
Figure 28: Microscope Image of the Tip of Coated Fiber After CVD Processing.....	56
Figure 29: SEM Image of the Probe Tip Attached to Carbon Paste.....	57
Figure 30: SEM Image of Platinum Deposits on the Fiber and the Trench. ....	58
Figure 31: SEM Image of a Gold-Coated Fiber Attached to Shuttle. ....	59
Figure 32: Depiction of Fiber Bonding Setup for Placing an Input/Output Fiber on Device. ....	60
Figure 33: Microscope Image of Completed Device.....	61
Figure 34: Depiction of Experimental Setup for Tests Performed in SEM.....	63
Figure 35: SEM Images of the Rear of the Shuttle.....	64
Figure 36: SEM Images of the Front of the Shuttle.....	65
Figure 37: Depiction of Experimental Setup Used to Test the Actuator in Air. ....	67
Figure 38: Image of Fibers Attached to the Thermal Actuator. ....	68
Figure 39: Data of the Reflected Spectrum from the Fabry-Pérot Cavity.....	68
Figure 40: 3D Geometry used in FEA Simulation. ....	71
Figure 41: Mesh used for the FEA Simulation. ....	71
Figure 42: Thermally Dependent Material Properties of Single Crystal Silicon.....	73
Figure 43: Temperature Gradients and Deformation at Various Applied Currents. ....	74
Figure 44: Temperature Distribution Along the Legs and Shuttle of the Actuator. ....	75
Figure 45: Out of Plane Deformation of the Shuttle at Various Applied Currents. ....	76
Figure 46: Plot of MATLAB Code that Determines Minima of Fringes in a Given Data Set. ....	78
Figure 47: Plot of $R^2$ Values of Curve Fits as Cavity Length and Cavity Finesse Value Vary.....	82
Figure 48: Equation Best-Fit Plotted Along With Data at 0 mA.....	83

Figure 49: Displacement of Front/Rear of Shuttle vs. Applied Current of SEM Data & FEA.....86  
Figure 50: Displacement vs. Current Plot Derived from Fabry-Pérot Cavity Data.....88

## **Chapter 1: Introduction**

In this chapter, the background and motivation for the work done in this thesis is presented followed by the objective of the thesis and concluding with a section showing the organization of the rest of the document.

### **1.1 Background and Motivation**

#### **1.1.1 Background**

In the years since Dr. Richard P. Feynman's talk in 1960 titled "There's Plenty of Room at the Bottom", which is often cited as the catalyst for the micro and nanoscience fields, MEMS devices have become ubiquitous in consumer products [1]. MEMS devices such as accelerometers, gyroscopic sensors, MEMS microphones, and more are found in cellphones, computing and entertainment input devices, and in the navigation systems of a multitude of transportation systems.

#### **1.1.2 Motivation**

There is a growing need to test the properties of materials at the micro and nanoscale due to their use in various applications, such as the structural material of MEMS devices. In 1961, Marsh et al. demonstrated an early micro-tensile testing machine that can measure extensions of a material from a few angstroms up to 15 mm of a thread with a cross sectional area of  $0.1 \mu m^2$  [2]. More recently, Zhu et al. presented a nano-tensile testing device based on thermal actuators [3]. The work done by Zhu has been improved on by Abbas et al. In work done by Abbas et al. the material tester is based on cascaded thermal actuators. Cascaded actuators allow for higher displacement and mitigate sample

heating issues encountered in previous work [4]. In both cases, the designs can be further improved with a more precise method of determining the displacement of the sample during testing. Lin et al. proposed the use of a fiber based Fabry-Pérot device for measuring displacement and shear stresses, but the FP cavity was not attached to a MEMS actuation method [5]. The device proposed in this thesis could similarly be used in the design of a robust nanomaterial testing system.

The design shown in this thesis could also be used as a displacement sensing system for obtaining closed loop control of MEMS devices designed for precision alignment tasks such as the following examples. Unamuno et al. demonstrated a precision alignment device based on thermal actuators for use in aligning bare fiber optic cables to one another or fibers to a chip containing optical waveguides [6]. Adding closed loop control via displacement measurements would improve the alignment capabilities of this device.

Another type of device that would benefit from a displacement sensing method is multi degree of freedom micro stages. By using multiple actuators connected to a single platform it is possible to make micro stages that have multi-degrees of freedom (DoF). These multi-DoF stages have many applications where having a method of displacement sensing would be useful. Multi-DoF stages have applications in biomedical research [7–9], micro-assembly of novel devices [7,9], scanning probe microscopy [9,10], probe-based computer file storage devices [11], and even as an image stabilization system for the CCD chips in cell phones [12]. A literature review on the challenges of microactuators for use in the above applications explicitly states the need for better sensing and control schemes to account for possible disturbances [9].

The original application of the device shown in this thesis is creating a tunable fiber based Fabry-Pérot cavity for use in cavity quantum electrodynamics experiments (CQED). In CQED experiments, the cavity is used as an atom trap. There are many examples of fiber based Fabry-Pérot cavities that are used in CQED experiments [13–16]. Steinmetz et al. noted in a recent paper that “while microscopic cavities are being actively developed, existing designs typically lack an easy way of tuning the cavity into resonance” [15]. Recently, Derntl et al. presented an array of tunable cavities made from electrostatically actuated cantilevers that have spherical mirrors etched into the ends of the cantilevers [17]. The thermally actuated fiber based Fabry-Pérot MEMS interferometer described in this thesis could also tune the cavity resonance by changing the length of the cavity. Other static designs used for CQED experiments, such as microdisk resonators, require the cavity to be physically etched in order to fine-tune the resonance before experiments can be performed [18,19].

## **1.2 Objective**

This thesis presents a thermally actuated fiber based Fabry-Pérot device that could be used as the basis of more complicated MEMS devices such as nanomaterial characterization system or as a tunable atom/ion trap for use in CQED experiments. The thermal actuator is created using traditional microfabrication processes. The mirrors that make up the Fabry-Pérot cavity are made from flat cleaved optical fibers. An alignment trench built into the thermal actuator is used to aid in placing the fiber mirrors onto the actuator. The performance of the thermal actuator is characterized both with and without the Fabry-Pérot cavity attached in separate experiments.

### **1.3 Organization of the Document**

The organization of this thesis is as follows. Chapter 2 introduces the theory of thermal actuators and Fabry-Pérot cavities. Chapter 3 discusses the design of thermal actuator and fiber based Fabry-Pérot cavity used in this thesis. Chapter 4 explains the processes used to fabricate thermal actuators, fiber mirrors, and details methods used to attach the fibers to the thermal actuator. Chapter 5 discusses the testing setups and procedures used to test the thermal actuator alone and the thermal actuator with the Fabry-Pérot cavity attached. Chapter 6 presents the multiphysics FEA model of thermal actuators and the MATLAB model of Fabry-Pérot cavities. Chapter 7 presents the results from the experiments performed on the thermal actuator and Fabry-Pérot cavity matched up with the corresponding results from the FEA and MATLAB simulations. Finally, Chapter 8 provides a summary of the work done in this thesis and offers a discussion on future work that can be done to improve the next iteration of this device.

## **Chapter 2: Theory of Thermal Actuators and Fabry-Pérot Cavities**

This chapter focuses on the theory underlying the operation of the thermally actuated Fabry-Pérot interferometer. The chapter is split into two parts: one section that focuses on the theory of thermal actuators and another section that focuses on the theory of Fabry-Pérot cavities. The section on thermal actuators is further split into two parts: one part on heat transfer that occurs during operation and another that focuses on the mechanical constraints that cause the actuator to move rectilinearly when heated. The section on the theory of Fabry-Pérot cavities gives an overview of the equations used to model the fringe pattern of a Fabry-Pérot cavity as well as the important design parameters of the cavity. The proceeding chapter goes into the design of the thermal actuator and the Fabry-Pérot cavity used in this project in more detail.

### **2.1 Theory of the Operation of Thermal Actuators**

All types of thermal actuators utilize mechanically constrained thermal expansion, typically induced via Joule heating, to achieve motion in the unconstrained directions of the device. Examples of thermal actuators include bimorph actuators, pseudo-bimorph actuators, and the style used in this design, chevron thermal actuators. Bimorph actuators are composed of a beam of two or more layers of material that have mismatched coefficients of thermal expansion (CTE) and are cantilevered at one end. Figure 1 shows a depiction of a bimorph actuator.



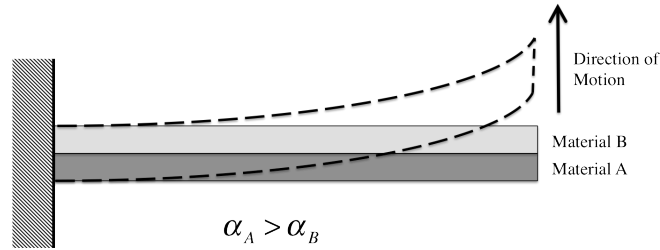


**Figure 1: Depiction of the Operation of a Bimorph Actuator. The Coefficient of Thermal Expansion (CTE) mismatch between material A and material B causes the beam to bend upward when heated.**

When heated, the materials expand at different rates causing the actuator to move towards the material layer with the lower CTE. Timoshenko’s work on bi-metal thermostats can be considered a precedent for bimorph actuators [20]. Additionally, there are several interesting MEMS applications for these devices such as artificial muscles, micro positioning, and other applications [21,22].

Pseudo-bimorph actuators work in a similar manner, but are composed of only one material. Pseudo-bimorphs are composed of two arms that have differing cross-sectional areas. The arm with the smaller cross-sectional area, known as the hot arm, has a higher resistivity than the arm with a larger cross-sectional area, called the cold arm. When a voltage is applied to the device, the hot arm expands more than the cold arm causing the arm to bend. The actuator bends in the direction of the cold arm. In Figure 2, a depiction of a pseudo-bimorph is shown. Several papers have investigated the operation and potential applications of these devices [23,24].

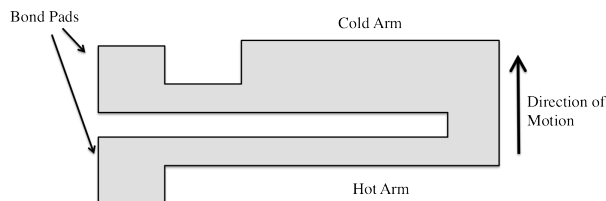


**Figure 2: Depiction of the Operation of a Pseudo-Bimorph Actuator. The temperature difference between the two arms of the actuator, due to different arm widths, causes the actuator to bend when heated.**

The type of actuator used in this project is the chevron thermal actuator. A chevron actuator consists of v-shaped beams that are connected to a central shuttle. Applying a differential voltage between the bond pads causes Joule heating and subsequent expansion of the arms of the actuator. Due to the constraints on the arms, the shuttle translates linearly. Figure 3 presents a depiction of a chevron thermal actuator.

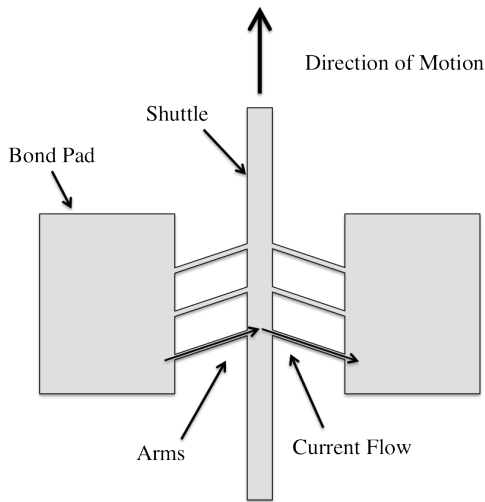


**Figure 3: Depiction of the Operation of a Chevron Thermal Actuator (TA). Current applied to the bond pads cause the actuator arms to heat and expand. The central shuttle moves linearly due to the initial bias of the actuator arms. A chevron TA is the type of actuator employed in this thesis.**

Multiple sets of chevron beams can be added to increase the force output of the actuator. Actuators can also be cascaded together to achieve large displacement capabilities [4,25–27].

The next subsection discusses general design parameters of a chevron thermal actuator and how each of these parameters affects maximum displacement and force output of the actuator. For the remainder of this document, the title chevron thermal actuator is shortened to thermal actuator (TA) or is simply referred to as the actuator or the device. The phrase “the device” can also refer to the thermal actuator with the Fabry-Pérot (FP) cavity installed.

### **2.1.1 Design Parameters of a Chevron Thermal Actuator**

Before delving into the details of the thermo-mechanical models used to simulate the behavior of chevron thermal actuators, it is useful to discuss the design parameters of this type of actuator. In general, there is a trade off between maximum force output and maximum displacement when designing a thermal actuator. The design parameters are the arm length, the cross-sectional area of the arms, the initial angle of the arms, and the number of sets of legs in the device. To increase the maximum displacement of a chevron TA, one can increase the arm length or reduce the initial angle of the arms. The drawback to increasing the arm length or reducing the initial angle of the arms is that these changes result in a decrease in the maximum force of the actuator. As mentioned before, one can also cascade multiple chevron devices to multiply the displacement output, however a detailed discussion on this subject is outside the scope of this thesis [4,25–27]. A method of increasing force output of the actuator without affecting maximum displacement is to increase the cross-sectional area of the arms and/or to increase the number of sets of arms that the device contains. The maximum force increases linearly with the number of sets of arms [28,29].

The above discussion provides general guidelines for designing chevron thermal actuators, however accurately modeling a thermal actuator is difficult due to the inherently non-linear nature of thermal actuators [30]. Finite-difference models, FEA models, and combinations of the two have been developed to accurately model thermal actuators. The next section discusses some of the models for simulating behavior of thermal actuators found in literature.

## **2.1.2 Analytical Models of Thermal Actuators**

To model a thermal actuator, it is necessary to treat the problem as a coupled thermo-mechanical system. Many papers focus exclusively on analytical models of the heat transfer problem and compare an analytical model to the temperature distribution found by FEA [27,31,32] and experiment [28,30]. Some papers use an analytical heat transfer model as the input for a mechanical FEA model [27,30]. There are also papers that assume that the temperature profile of the actuator is known and focus on creating analytical finite difference solutions to the mechanical system of the actuator [3,4]. Other papers derive analytical finite difference models of both the thermal and mechanical problems [26,29,33–35]. The next subsection details commonly cited analytical models of both the heat transfer and mechanical simulations in separate sections starting with the heat transfer problem. Within each of the two sections, the simplest models are presented first, leading to the more nuanced models found in literature. After discussing methods used to obtain the temperature profile of the chevron arms of thermal actuators, common methods used to model the mechanics of actuators found in literature are shown.

### **2.1.2.1 Heat Transfer Models Found in Literature**

In order to model a temperature distribution along the arms of a chevron thermal actuator one needs to first define the types of heat transfer that take place during the operation of the device. The resulting heat transfer balance can be solved by writing a finite difference code to obtain a temperature distribution [27,30,32] or by deriving an explicit function for the temperature distribution [28,29,33–35]. In some cases, an explicit function for the temperature distribution must also be solved using a finite difference code.

This subsection is further split into two parts; one that details the types of heat transfer that occur in thermal actuators and another subsection that discusses the methods of using the heat transfer balance to obtain a temperature distribution along the actuator arms.

### 2.1.2.1.1 Heat Transfer Balance in a Thermal Actuator

The most comprehensive model contains all of the following heat transfer modes in a given thermal actuator system. Figure 4 shows all of the possible heat transfer modes that affect a given element volume within the arm of a TA.

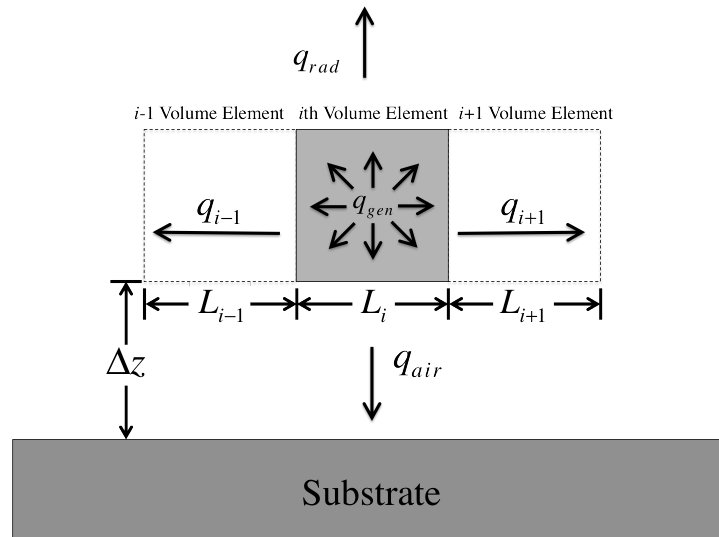


**Figure 4: Diagram Representing Modes of Heat Transfer in a Volume Element in a TA. In this figure,  $q_{gen}$  is the heat generated via Joule heating,  $q_{i\pm 1}$  is heat conduction between the volume elements,  $q_{air}$  is heat conducted to the air, and  $q_{rad}$  is the radiative heat loss term. The figure also shows relevant dimensions that are used in the equations throughout this chapter.**

As shown in Figure 4, heat is generated internally,  $q_{gen}$ , via Joule heating. Conduction from one adjacent element to the next is represented by  $q_{i\pm 1}$ . For experiments performed in air, heat is removed by conduction to the air as represented by  $q_{air}$ . A small amount of heat is transferred to the surrounding via radiative cooling,  $q_{rad}$ . In the case of DC Joule

heating, the system is in a steady-state equilibrium and can be defined by the following equation.

$$q_{gen} + q_{i\pm 1} + q_{air} + q_{rad} = 0$$

In the case of AC Joule heating or pulsed power testing, the above heat flux balance would be equal to a term representing the storage of thermal energy within the given volume element [24,25,28,29,32]. While a detailed discussion of AC actuation is outside the scope of this thesis, it is still useful to discuss the temporally independent aspects of approaches contained in the papers that consider AC Joule heating.

The remainder of this section discusses various ways that each heat transfer terms are modeled in literature. This section is organized by starting from the left hand side of the equation representing the heat flux balance and proceeding sequentially to the next term in the equation. The proceeding section looks at the resulting explicit temperature profile equations that can be determined from the heat flux equation.

#### **2.1.2.1.1.1 Common Descriptions of Internal Heat Flux**

Heat flux generated by Joule heating can be represented in terms of voltage as shown below [29,32,35].

$$q_{gen} = \frac{V^2}{R_{act} \forall_i}$$

Where  $V$  is the voltage applied to the actuator,  $\forall_i$  is the volume of the element node in question and  $R_{act}$  is the resistivity of the actuator.

Internal heat flux can also be represented in terms of current as shown in the following equation [27,28,30].

$$q_{gen} = \frac{\rho_{act} \times L_i \times i^2}{A_x}$$

In this expression,  $\rho_{act}$  refers to the resistivity of the material that makes up the thermal actuator,  $L_i$  is the length of the volume element and  $A_x$  is the cross sectional area of the actuator arm.

Some papers use constant values for the resistivity of the actuator material[29,32,35]. Multiple papers use a temperature dependent expression for the resistivity of the actuator material [27,28,30,34]. Baker et al. and Howell et al. both use an empirically determined temperature dependent expression for the resistivity of the actuator material [27,30]. Both Enikov et al. and C.D. Lott use a linear approximation for a temperature dependent expression for resistivity that is derived using the materials temperature coefficient of resistance,  $\beta$ , as shown in the equation below [28,34].

$$\rho_{act} = \rho_o (1 + \beta(T_i + T_{sub}))$$

In the linear approximation shown above,  $\rho_o$  is the resistivity of the material at room temperature,  $T_i$  is the temperature of the volume element and  $T_{sub}$  is the temperature of the substrate.

#### **2.1.2.1.1.2 Common Descriptions of Heat Conduction Within a Actuator**

The next mode of heat transfer to discuss is heat conduction within the actuator between the volume elements. Girbau et al. uses the following form shown below.

$$q_{i\pm 1} = \frac{\partial}{\partial x} \left( k_{act} \frac{dT}{dx} \right)$$

In this equation,  $k_{act}$  is the thermal conductivity of the actuator material [29].

It is more common for conduction between the nodes that make up the actuator arm to be represented by the following expression.

$$q_{i\pm 1} = \frac{k_{act} A_x}{L_i} (T_{i\pm 1} - T_i)$$

In the above equation,  $A_x$  is the cross sectional area of the actuator arm,  $L_i$  is the length of the node element,  $T_{i\pm 1}$  is the temperature of the adjacent element and  $T_i$  is the temperature of the element in question [27,28,30].

Several papers consider  $k_{act}$  as being thermally independent in their models [28,29,32–35]. Others use a thermally dependent expression for  $k_{act}$  that is empirically determined from experiment [28,30].

#### **2.1.2.1.1.3 Heat Transfer to the Air From the Actuator in Atmospheric Tests**

When thermal actuators are tested in air, there is heat transfer to the air from the actuator arms. For MEMS devices, conduction to the air dominates over natural convection because the air flow is quasi-static [32]. Hickey et al. argues that conduction is the dominant heat transfer process over convection by computing the Rayleigh number for the dimensions of a typical thermal actuator. The Rayleigh number (Ra) is the ratio of the buoyancy and the viscosity forces of a fluid multiplied by the ratio of the momentum and thermal diffusivities of a fluid for a given surface [36]. On macroscopic scales, Ra numbers of the magnitude of  $10^5$  indicate that natural convection is the primary mode of heat transfer [32]. Hickey et al. computed the Ra number for a 2-micron wide arm at 500 °C to be  $Ra \approx 3 \times 10^{-8}$ . Because the Ra number for a thermal actuator is small, the effects of natural convection can be considered to be negligible [32].



Hickey et al. also argues that a 1D model of the actuator arm is permissible by calculating the Biot number (Bi) for a typical thermal actuator system. The Biot number is a dimensionless parameter representing the ratio of heat transfer resistances inside of a body vs. the surface of the body. For  $Bi \leq 0.1$ , the temperature gradient with a given body is slight and can thus be approximated as being at a uniform temperature [32,36]. The Biot number for typical thermal actuator dimensions is in the range of  $Bi \approx 0.0006$  and hence the use of a 1D heat transfer approximation is permissible [32].

Conduction of heat to the air and into the substrate from the actuator arms is typically treated as steady heat conduction through a plane wall. The most general equation for conduction of heat through a material can be described as follows.

$$q_{wall} = k_{eff} A_{wall} \frac{\Delta T_{wall}}{L_{wall}}$$

In this equation,  $k_{eff}$  is the average thermal conductivity of the entire wall,  $A_{wall}$  is the cross-sectional area of the wall that is perpendicular to heat flux,  $L_{wall}$  is the thickness of the wall through which heat flux propagates and  $\Delta T_{wall}$  is the temperature difference between the planes that define the ends of the wall. In the case of a thermal actuator, the wall can be defined as the air between the bottom of the actuator arm and top of the substrate. Some models have additional terms of thermal resistances between the air and the substrate to account for thin film materials that are on top of the substrate as a result of the chosen manufacturing process [28,34].

Because of the complicated geometry of thermal actuators, a conduction shape factor is commonly employed to determine the heat conduction from the actuator beams to the surrounding air and substrate [27,28,30,34].

Hickey et al. uses a simplistic effective conduction shape factor. The shape factor is approximated as one half the cross-sectional perimeter of the actuator arm. In Hickey's model, heat transfer to the air via conduction is defined as follows [32].

$$q_{air} = \frac{k_{air}}{\Delta z} \cdot \frac{P_{b_i}}{2} \cdot L_i (T_i - T_{sub})$$

In this equation,  $k_{air}$  is the thermal conductivity of air,  $\Delta z$  is the length of the gap between the actuator arms and the substrate,  $L_i$  is the length of the element of the actuator arm,  $P_{b_i}$  is the perimeter of the bottom of an element of the actuator arm,  $T_i$  is the average temperature of the element, and  $T_{sub}$  is the average temperature of the substrate. Lai et al. also uses this form for heat conduction to the air from in their model [35].

A more common form of defining heat conducted to the air that several papers utilize in their models is as follows:

$$q_{air} = \frac{S k_{air} A_{b_i}}{\Delta z} (T_i - T_{sub})$$

In the equation above,  $S$  is the conduction shape factor and  $A_{b_i}$  is the area of the bottom surface of the element of the actuator arm and the other terms are as previously defined [27,28,30,34]. Several papers that use this form for heat conduction also use the following shape factor defined below [27,28,34].

$$S = \frac{t}{w} \left[ \frac{2\Delta z}{t} + 1 \right] + 1$$

In this expression,  $w$  and  $t$  are the length and width of the actuator arm. Lin et al. determined this shape factor for a suspended polysilicon beam using a FEA simulation.

The FEA derived shape factor was then validated with data obtained from an experiment involving a Joule heated polysilicon beam immersed in an electronic cooling liquid [37].

It is important to note that almost all of the papers mentioned treat  $k_{air}$  as a constant. C.D. Lott et al. and Baker et al. model  $k_{air}$  as a linear function of temperature and found that using a temperature dependent  $k_{air}$  affects the model behavior more than using a temperature dependent  $k_{act}$ , the thermal conductivity of the actuator material [28,30].

#### 2.1.2.1.1.4 Common Descriptions of Radiative Heat Transfer to the Surroundings

The last mode of heat transfer to be discussed is radiative heat transfer from the actuator arms to the surroundings. Radiative heat flux is defined by the following equation.

$$q_{rad} = \epsilon_{act} \sigma A_{s_i} (T_{sub}^4 - T_i^4)$$

In this equation,  $\epsilon_{act}$  is the emissivity of the actuator material,  $\sigma$  is the Stefan-Boltzmann constant, and  $A_{s_i}$  is surface area of the beam element excluding the sides involved with heat conduction between elements. Baker et al. and Lott et al. both include radiative heat transfer in their model [28,30]. Baker found that radiative heat transfer is not a significant factor. Hickey et al. argues that compared to heat transfer to the air, that even at very high temperatures (1000 °C), less than %1 of heat is lost to the surroundings due to radiation [32]. Operating temperatures of thermal actuators are generally lower than 1000 °C. Baker et al. found that a thermal actuator operating constantly at a maximum temperature of 650 °C over 6 days will cause a oxide film to form over the actuator arms [30]. This observation shows that there is an effective limit to the operating temperatures of thermal actuators and hence radiative heat loss can be neglected.

### **2.1.2.1.2 Methods of Obtaining a Temperature Profile of the Actuator**

By using some or all of the heat transfer terms outlined in the previous section, along with temperature boundary conditions, it is possible to calculate temperature profiles of the thermal actuator arms. The main boundary condition is that the temperature of the substrate  $T_{sub}$  remains at room temperature throughout the simulation.

Two common methods used in literature for obtaining temperature of the arms is to either use a finite difference code to iteratively solve the heat flux equation [27,30–32] or to derive an explicit equation for temperature by solving the heat balance differential equation for temperature [28,29,34,35]. The finite difference method is briefly mentioned in the next section followed by a section that shows several different explicit formulas for obtaining temperature along actuator arms.

#### **2.1.2.1.2.1 Finite Difference Method of Obtaining a Temperature Profile**

Baker et al. uses a finite difference code that incorporates all of the modes of heat transfer mentioned in the previous section. Finite difference code used by Baker et al. also incorporates temperature dependent expressions for resistivity, thermal conductivity, the coefficient of thermal expansion of the actuator material and a temperature dependent expression for the thermal conductivity of air. The finite difference model shows good agreement with experiments. Baker's model for the temperature profile of the actuator arms match well with temperature measurements made using infrared imaging taken during experiment [30]. Hickey et al. and Matmat et al. also solve for the temperature distribution using custom finite difference code but neither use temperature dependent material properties in their simulations or compare the temperature distribution from simulation to experimental results [31,32].

### 2.1.2.1.2.2 Explicit Forms of the Temperature Distribution

In this section, basic methods of obtaining an explicit temperature distribution of an actuator arm are presented first followed by methods that more accurately represent the heat transfer that occurs during experiment.

One of the most straightforward explicit temperature distributions can be found by taking into account only internal heat generation by Joule heating and heat conduction within the actuator arm. Work done by Girbau et al. models an actuator in vacuum hence only the two aforementioned heat transfer terms are considered [29]. Disregarding heat conduction to the air from the actuator arms is applicable in the case where actuators are tested in a vacuum environment such as in an SEM microscope. The temperature distribution Girbau et al. determined is as follows.

$$T(x) = -\frac{q_{gen}}{2k_{act}}x^2 + \frac{q_{gen}}{2k_{act}}L \cdot x + T_{sub}$$

In this equation,  $T(x)$  is the temperature at a given position on the x-axis, which is oriented along the axis of the actuator arm,  $T_{sub}$  is the temperature of the substrate,  $q_{gen}$  is the internal heat flux caused by Joule heating,  $L$  is the length of the actuator arm from the bond pad to the shuttle, and  $k_{act}$  is the thermal conductivity of the actuator material. Girbau et al. used a constant, non-temperature dependent value for  $k_{act}$  their model. Kushkiev et al. used Girbau's model with constant material properties and temperature dependent material properties [33]. Kushkiev compared the constant and temperature dependent versions of Girbau's model to FEA. Kushkiev found that the original model using constant thermal material properties undershot the FEA model by 30%. By adding temperature dependent expressions for material properties to the model by Girbau et al.,

the results of the simulation with temperature dependent materials match the FEA with <2.2% error [33]. The work done by Kushkiev et al. demonstrates that a simple model combined with temperature dependent material properties can be used to aid in designing thermal actuators that would be used in vacuum.

While a model that ignores conduction of heat from the actuator arms to the air is valid for cases where the actuator is tested in vacuum, such as testing the device in an SEM, it is desirable to find an explicit temperature function for the case where the actuator is tested in air. The remaining examples in this section focus on temperature functions that take air conduction into account.

The explicit temperature distribution in work done by Lott et al. is time dependent because Lott performed AC experiments on their actuators. Because AC testing is outside the scope of this thesis, the explicit temp distribution is omitted [28]. It is useful however to discuss the modeling of constant material properties vs. temperature dependent material properties that Lott et al performed in their work. To determine the relative importance of thermal conductivity of the actuator material vs. thermal conductivity of the air, three cases were examined: one where both the conductivity of the actuator is held constant,  $k_{act} = \text{constant}$  and the conductivity of the air is held constant,  $k_{air} = \text{constant}$ . Another model is created where conductivity of the air is modeled as a function of temperature,  $k_{air}(T)$ , while conductivity of the actuator remains constant,  $k_{act} = \text{constant}$ . Finally, a third case where both conductivity of the air is temperature dependent,  $k_{air}(T)$ , and conductivity of the actuator are temperature dependent,  $k_{act}(T)$ . Comparing the resulting temperature profiles from the three cases above, Lott et al. found that a temperature dependent conductivity of air is a dominating factor compared to a

temperature dependent conductivity of the actuator material [28]. Lott et al. were not able to measure the temperatures of their actuators directly to validate their temperature model and instead compare their model to the results from an FEA model [28].

Another model that accounts for conduction of heat from the actuator arms to the air is found in work done by Lai et al. Lai et al. cites the heat transfer balance from Hickey et al. but solves the differential equation to solve for an explicit expression of the temperature of the actuator [35]. The heat transfer balance that Hickey et al. uses takes into account internal heat generation, heat conduction through the actuator arms and heat conduction to the air [32]. In solving the heat transfer balance using the aforementioned boundary conditions, Lai et al. defines the temperature along the actuator arm as follows.

$$T(x) = 1 - \frac{\cosh(\sqrt{\omega}x)}{\cosh(\sqrt{\omega}L)} \cdot \frac{\Delta z}{k_{air} \frac{P_{b_i}}{2L}} \cdot \frac{V^2}{R_{act}}$$

In this equation,  $T(x)$  is the temperature at a point  $x$  which lies on an axis oriented along the actuator arm,  $L$  is the length of one arm from bond pad to shuttle,  $\Delta z$  is the length of the air gap between the bottom of the actuator and the substrate,  $k_{air}$  is the thermal conductivity of the air,  $P_{b_i}$  is the perimeter of the bottom of an element of the actuator arm,  $V$  is the voltage applied to the actuator and  $R_{act}$  represents the resistance of the actuator arm. The remaining parameter  $\omega$  is defined as follows.

$$\omega = \frac{k_{air} \cdot \frac{P_{b_i}}{2}}{A_x \cdot k_{act} \cdot L}$$

In this expression,  $A_x$  is the cross sectional area of the actuator arm and  $k_{act}$  is the thermal conductivity of the actuator material.

The material properties in this model,  $k_{air}$ ,  $k_{act}$  and  $R$  are all constants and do not vary with temperature. Lai et al. did not compare the above explicit temperature distribution to FEA or directly to experimental data [35].

One of the most detailed temperature expressions is derived by Enikov et al. Enikov et al. base their model on the energy balance found in the work done by Lott et al. [28]. The heat transfer balance utilized by Lott et al. takes into account internal heat generation, heat conduction within the actuator arm, heat conduction to the air, and radiative heat transfer. Enikov et al. drops the radiative heat transfer terms and the time dependent terms used by Lott et al. and derives an explicit function describing the average temperature of the actuator arms. Enikov et al. introduces a term,  $\gamma$  which represents the relative magnitude of the Joule heating vs. the heat flux out of the actuator for a given temperature. For the case of  $\gamma > 0$  more heat is generated by internal heating than is being removed by conduction to the air and for  $\gamma < 0$  the opposite is true. The parameter  $\gamma$  is defined by the following expression.

$$\gamma = \frac{i^2 \rho_{act} \beta}{w^2 t^2 k_{act}} - \frac{S \cdot k_{air}}{\Delta z \cdot t \cdot k_{act}}$$

In this expression,  $\rho_{act}$  is the resistivity of the actuator material,  $w$  and  $t$  are the length and width of the actuator arm,  $S$  is the shape factor from Lin et al. [37],  $i$  is the applied current, and  $\beta$  is the temperature coefficient of resistance of the actuator material.

The explicit expression for the average temperature depends on the sign of  $\gamma$ . For  $\gamma > 0$  the temperature expression is harmonic and for  $\gamma < 0$  the temperature expression is hyperbolic [34]. The temperature expression is defined below.



$$T_{ave} = \begin{cases} \frac{i^2 \rho_{act}}{\gamma w^2 t^2 k_{act}} \cdot \left( \frac{\tan(\sqrt{\gamma} L)}{\sqrt{\gamma} L} - 1 \right) & \gamma > 0 \\ \frac{i^2 \rho_{act}}{\gamma w^2 t^2 k_{act}} \cdot \left( \frac{\tan(\sqrt{|\gamma|} L)}{\sqrt{|\gamma|} L} - 1 \right) & \gamma < 0 \end{cases}$$

The variables in the above expression are the same as defined for the terms in  $\gamma$ . All of the material properties in this model are assumed to be constant and do not change with temperature [34].

When compared to FEA results, the analytical expression above matched FEA with 1.1% error and also closely match experimental results despite using non-temperature dependent material properties [34].

It should be noted that the temperatures in the experiment, FEA, and the analytical model ranged from 25 ° C up to 300 ° C in the work done by Enikov et al. [34]. In other literature, the maximum operating temperature of the actuator is over twice the maximum temperature cited in the experiments of Enikov et al.. It is conceivable that at higher temperatures, the analytical and FEA model would start to deviate from the experimental data due to the omission of temperature dependent models as shown in other papers [27,29,30,33].

### 2.1.2.2 Various Analytical Mechanical Models of Thermal Actuators

Knowing the average temperature of the thermal actuator arm, it is possible to model displacement of the thermal actuator. In literature, methods of determining the displacement of a thermal actuator for given temperatures range from purely geometrical arguments [29,35] to beam bending models [3,25,34]. Others model the temperature

distribution analytically and pass those results to an FEA model [27,30] or perform both the thermal and mechanical modeling using a multiphysics FEA [31,33]. This section focuses on analytical models found in literature starting with models based on geometrical arguments and proceeding to beam deformation models.

### 2.1.2.2.1 Purely Geometrical Models

Both Girbau et al. and Lai et al. use purely geometrical arguments to model displacement of a thermal actuator [29,35]. The papers assume that the actuator beam and actuator move linearly in the direction of the pre bend of the actuator arm as shown in Figure 5.

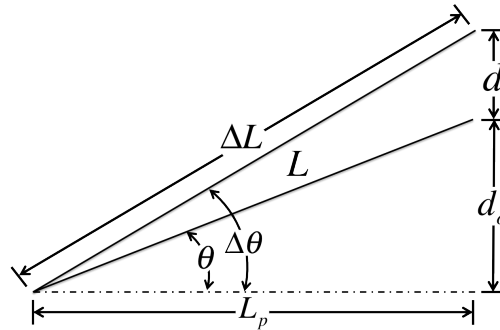


**Figure 5: Model of the Kinetics of a Thermal Actuator. In this model, only the geometry defined in the figure and the definition for thermal expansion is used to determine the displacement of the actuator. The dimensions with the  $\Delta$  prefix represent the geometry of the actuator after motion and the dimensions without the prefix denote the initial geometry of the device.**

Girbau et al. explicitly found the average temperature of the actuator arms as discussed in the previous section on obtaining a temperature profile of the actuator [29]. Using the average temperature of the actuator arm,  $\Delta T$ , it is possible to calculate the change in length,  $\Delta L$ , of the arm as a result of thermal expansion of the material. By computing the average of the temperature, the change in length of the actuator arms can be found as follows [29].

$$\Delta L = \alpha_{act} \int_0^L \Delta T dx = \frac{\alpha_{act} q_{gen} L^3}{12k_{act}}$$

In this equation,  $\alpha_{act}$  is the coefficient of thermal expansion of the actuator material, and  $q_{gen}$ ,  $k_{act}$  and  $L$  are as defined earlier. To find displacement, one uses the assumptions mentioned before, that the actuator moves linearly in the direction of the bent beam, along with the geometry shown in Figure 5, to compute displacement of the actuator. According to this method, displacement of the actuator can be approximated as follows.

$$d = \left[ \frac{L + \Delta L}{2} \right] \sin \left[ \cos^{-1} \left( \frac{2L_p}{L + \Delta L} \right) \right] - d_0$$

In this equation,  $d$  is the displacement of the actuator,  $L_p$  is the projected length of the actuator, while  $L$  and  $\Delta L$  are as previously defined.

As mentioned before, Girbau et al. used constant material properties for  $\alpha_{act}$  and  $k_{act}$  [29]. The model was found to have good agreement with an FEA model.

As previously mentioned, Kushkiev et al. compared the work done by Girbau et al. using constant material properties and temperature dependent material properties to an FEA model. Using temperature dependent material properties, the analytical model had <2% error compared to FEA. Using constant material properties, the displacement was lower by than the FEA model 30% [33].

Lai et al. used the same geometric assumptions found in Figure 5. Instead of finding the displacement however, Lai et al. derives a geometric relation which can be used to estimate the motion amplification of an actuator for a given projected length and initial vertical height. The relation, titled Geometric Amplification, or  $G.A.$ , is as follows.

$$G.A. = L_p / d_0$$

In this equation,  $G.A.$  stands for Geometric Amplification and the other variables are as shown in Figure 5. Lai compared the geometric amplification predicted from this equation with the simulation results done by Hickey et al. Lai found that the simulated displacements from Hickey et al. are proportional to the expression for geometric amplification [35].

#### **2.1.2.2.2 Beam Deformation Models**

While purely geometrically based arguments are useful in aiding the design of actuators that operate at low temperatures and small displacements, it is necessary to take into account how the mechanical constraints of the system affect the deformation of the actuator arms at high temperatures. This is accomplished by modeling the arms as a two dimensional beam problem. The remaining examples in this section focus on analytical equations for obtaining the displacement of the actuator that are derived from considering the actuator arm as a two dimensional beam.

The mechanical model in work done by Zhu et al. assumes a perfectly rigid central shuttle that is not affected by temperature. The model also assumes small displacements, ignores any reaction moments and assumes the actuator has infinite shear stiffness [3]. A free body diagram showing the loading considered in this model is shown in Figure 6.

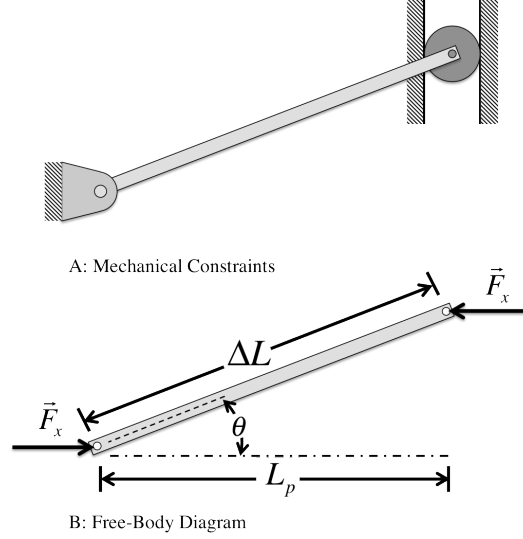


**Figure 6: Mechanical Constraints & Free-Body Diagram Relating to Work by Zhu et al.** As shown in the top insert, the constraint at the bond pad is considered as a pin joint. The constraint at the shuttle is considered to be a roller in a slot. The bottom insert shows the resulting free body diagram. In this model, only forces in the x direction are supported by the constraints. While this description of the situation underestimates the constraints of the actual device, the simplifications make determining the displacement straightforward.

Using the aforementioned constraints shown in Figure 6, along with an average temperature determined from an FEA model, the displacement is as follows.

$$d = \alpha_{act} \Delta T \times L \left( \frac{\sin(\theta)}{\sin^2(\theta) + \cos^2(\theta) / \psi} \right)$$

In this expression  $\psi$  is defined as  $\psi = \frac{A_x L}{12I}$  where  $I$  is the area moment of inertia of the actuator arm [3]. While this model uses a temperature independent  $k_{act}$ , this model does include temperature dependent material properties for  $\alpha_{act}$  and  $\rho_{act}$ . The displacement model was compared to FEA and to data obtained from experiment. The analytical model showed slight deviations from both the experimental model and the FEA at high temperatures [3].

Que et al. also assumes rectilinear motion of the actuator and accounts for reaction forces at the boundaries of the actuator arms. The model also accounts for bending

moments from the cantilevered constraint of the arm fixed to the bond pad. The model from the work by Que et al. however, does not take lateral beam deformation due to bending moments into account. The displacement model is derived using beam-bending equations. The free body diagram for this case is shown in Figure 7 [25].

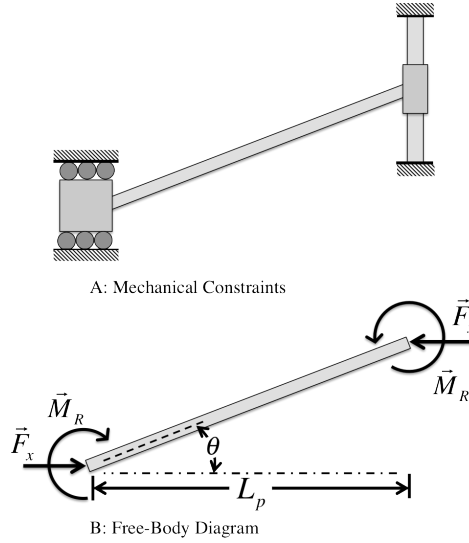


**Figure 7: Mechanical Constraints & Free-Body Diagram Relating to Work by Que et al.** The top insert shows the constraint at the bond pad modeled as if the actuator arm is welded to a roller in a horizontal slot. The other side of the actuator arm is welded to a ring that can move along a shaft. The resulting free body diagram shows that this model takes bending moments into account resulting in an overall stiffer model than the model by Zhu et al. shown in Figure 6.

The mechanical model that Que et al. uses shown in Figure 7 is based off of work done by Y.B. Gianchandani et al. on bent beam MEMS strain sensors [26]. Using the above assumptions and constraints, displacement of the shuttle can be expressed as follows.

$$d_{max} = 2 \frac{\tan(\theta)}{\xi} \tan\left(\frac{\xi L}{2}\right) - L \tan(\theta)$$

In this equation,  $d_{max}$  refers to the maximum displacement of the actuator in absence of an external loading [25]. The term  $\xi$  is defined as follows.

$$\xi = \sqrt{F_x / EI}$$

In this expression,  $F_x$  is the reaction force in the x direction at the bond pad as shown in Figure 7, E is the elastic modulus of the actuator material and I is the area moment of inertia of the actuator arm. In this model, all of the material properties do not vary with changes in temperature. The displacement model was found to be within 5% of the displacement found from FEA.

As mentioned in the section on obtaining explicit temperature distributions, one of the most comprehensive analytical models is found in work done by Enikov et al. The free body diagram detailing the loadings that are taken into account in this model is shown in Figure 8.

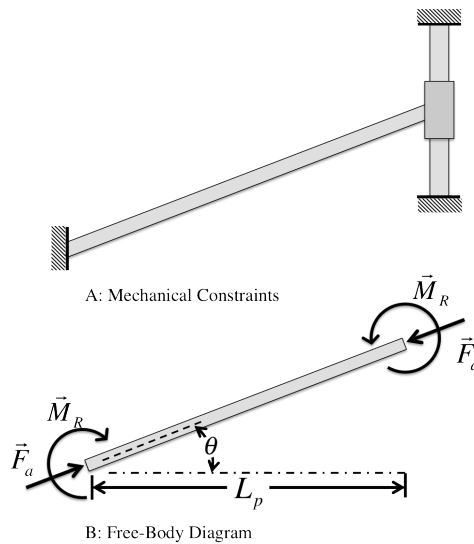


**Figure 8: Mechanical Constraints & Free-Body Diagram Relating to Work by Enikov et al. The top insert shows that the actuator arm is cantilevered to the bond pad. The other end of the arm is welded to a ring that can ride along a shaft. The bottom insert shows the resulting free body diagram. The model by Enikov et al. is the most comprehensive, but consequently, the most difficult to derive and implement for modeling the behavior of a TA.**

The actuator arm shown in Figure 8 is modeled as a constrained beam subjected to both compression and lateral bending. In this loading situation, the actuator arm can be represented as a beam column model. Using the beam-column model, displacement of the actuator can be expressed by the following equation.

$$d = \tan(\theta) \left( \frac{2 \tan\left(\frac{\xi L}{2}\right) - \xi L}{\xi \cos(\theta)} \right)$$

In this case,  $\xi$  is defined in a slightly different manner than is shown in the model from Que et al. The term  $\xi$  is defined by the following expression.

$$\xi = \sqrt{F_a / EI}$$

Where  $F_a$  is the reaction force from the bond pad on the actuator oriented to an axis along the actuator as shown in Figure 8.

A transcendental equation consisting of  $T_{ave}$  and  $\xi$  is used to determine the value of  $F_a$  allowing the displacement to be solved [34]. The average temperature of the actuator arms is determined from the expression that Enikov et al. derived, which was shown in the section on obtaining a temperature profile. The average temperature used in this model ranges from 25 ° C up to 300 ° C. All of the materials used in both the thermal and mechanical models by Enikov et al. are constant and do not vary with temperature.

When compared to FEA, at the maximum temperature considered of 300 ° C, the displacement from the analytical model was within 1.1% of the displacement determined by FEA. The analytical model also agrees well with the average temperatures and displacements found from experimental data. However, as mentioned before, the maximum temperature used in the work done by Enikov et al. is much lower than that of other papers. The analytical and FEA models in this work could deviate from experimental data at higher temperatures due to the lack of the use of temperature dependent material properties.



### **2.1.2.3 Final Remarks on Theory of Thermal Actuators**

Simple models (both mechanically and thermally) are good for designing and modeling thermal actuators that operate at low temperatures. The simplistic models are also shown to be more accurate when temperature dependent material properties are integrated into the model. More detail can be added to the model to more accurately reflect what happens during experiment, however this refined detail comes at the expense of less intuitive functions and reduced ease of implementation of the model.

This project utilizes a multiphysics FEA model that includes thermally dependent expressions for the material properties of the actuator material. The details of this FEA model are further discussed in chapter 6.

Having thoroughly discussed a multitude of different methods of modeling the thermal actuator, which is one half of the thermally actuated fiber based Fabry-Pérot interferometer, an overview of the theory of the Fabry-Pérot cavity remains to be discussed.

## **2.2 Theory of the Fabry-Pérot Cavity**

In this section, the theory behind Fabry-Pérot cavities is shown. The design parameters that affect the operation of the cavity are also discussed. The methods used to obtain displacement using a Fabry-Pérot cavity is discussed later in chapter 7 and in appendix 1.

As the name suggests, Fabry-Pérot cavities are based off of the work done by Charles Fabry and Alfred Pérot on a interferometric device in 1897 [38]. Fabry and Pérot used work by Boulluch et al. which was published in 1893 [38]. Boulluch et al. outlined a theory of fringe formation, which was in turn, based off of work done by Airy in 1836

[38]. Airy was the first to carry out the computation of multiple beams interfering between two infinitely thin plates [38]. Before the work done by Airy, the intensity of successive beams reflecting off of two opposing surfaces would be disregarded because glass has a low reflectivity and hence the light intensity falls off quickly with each succeeding reflection [38].

Early Fabry-Pérot interferometers consisted of silver coated glass wedges separated by two metal spacers that can be swapped out to change the length of the cavity [38]. A modern version of the parallel-plan Fabry-Pérot cavity used in this thesis is the Fiber based Fabry-Pérot Cavity (FFPC). A fiber based Fabry-Pérot cavity is made up of two cleaved optical fibers, or a cleaved optical fiber and a coated surface that is used as a mirror [5,39–42]. The gap between the two fibers is in some cases fixed, in which case the FFPC is called an etalon [13–15]. If the cavity length can be changed via pressure, a piezoelectric transducer, or a MEMS device, the FFPC is considered to be an interferometer [5,39–42]. There are other types of Fabry-Pérot cavity configurations other than parallel plane such as plane parallel mirror, concentric mirrors, confocal mirrors, hemispherical mirrors and others, however the discussions of these alternative types of cavity configurations are outside this scope of this thesis [13].

The following summarizes the basics of how airy intensity functions are derived. More comprehensive derivations can be found in books on optics and books about interferometers [38,43,44].

The cavity is modeled as two semi-transparent mirror that are separated a distance,  $d_{cav}$ , between mirror 1 and mirror 2 as shown in Figure 9.

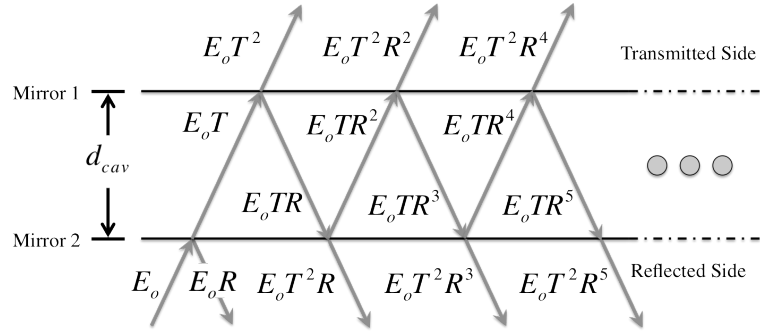


**Figure 9: Ray Optics Approach to Deriving the Equations for A Fabry-Perot Cavity.** The figure shows paths of light rays reflecting between two parallel infinitely long mirrors. A light beam enters from the bottom of the figure and is reflected inside the cavity. The multiple reflections form interference patterns on either sides of the cavity. The reflected interference pattern that would occur at the bottom mirror in this figure is what is measured in the experiments performed in this thesis.

Each mirror has a reflectivity  $R$  and a Transmittance  $T$ . In this ideal case, absorption of the mirrors is not considered. For the case where each mirror has different optical properties, the reflectivity and transmittance of the entire system is as follows [43,45].

$$R = \sqrt{R_1 R_2}$$

$$T = \sqrt{T_1 T_2}$$

In this expression  $R_1$  and  $T_1$  are the reflectivity and transmittance of mirror 1 while  $R_2$  and  $T_2$  are the reflectivity and transmittance of mirror 2.

From energy considerations, the sum of  $R$  and  $T$  is as follows.

$$R + T = 1$$

Additionally, if absorption is considered, the sum is instead the following.

$$A + R + T = 1$$

As depicted in Figure 9, refraction is not considered in this derivation. As a result of ignoring refraction, the angle between any given ray and the vertical is  $\phi$  as shown in Figure 9. The phase difference between any two adjacent beams can be expressed by the following equation [43,46].

$$\delta = \frac{4\pi}{\lambda} n \cdot d_{cav} \cdot \cos(\phi)$$

In the above equation,  $\lambda$  is the wavelength of light coming into the cavity,  $n$  is the index of refraction of the medium between the mirrors, which is typically air, and  $d_{cav}$  is the distance between the mirrors. Since there can be an additional phase change upon reflection,  $\delta_r$ , the total phase change between any two adjacent beams is expressed as the following [43].

$$\Delta = \delta + \delta_r$$

Expressing the phase change between any two adjacent beams as  $e^{j\delta}$  and summing successively transmitted/reflected rays, the amplitudes at the transmitted and reflected side of the mirrors can be defined by the following expressions [43].

$$E_T = E_0 T^2 + E_0 T^2 R^2 e^{j\delta} + E_0 T^2 R^4 e^{2j\delta} \dots$$

$$E_R = E_0 R + E_0 T^2 R e^{j\delta} + E_0 T^2 R^3 e^{2j\delta} \dots$$

In the above expressions,  $E_R$  and  $E_T$  are the resulting electric field for the reflected and transmitted sides of the mirror respectively,  $E_0$  is the initial electric field, and other values are as previously defined [43].

The expressions above can be more concisely defined by the following equations.

$$E_T = E_0 T^2 + \sum_{n=1}^{\infty} E_0 T^2 R^{2n} e^{nj\delta}$$

$$E_R = E_0 R + \sum_{n=1}^{\infty} E_0 T^2 R^{2n+1} e^{nj\delta}$$

By expanding the above equations as a geometric series, separating and equating the real and imaginary terms, and noting that intensity can be found by  $I = |E|^2$ , the intensity as viewed from the transmitted side of the cavity can be expressed by the following.

$$I_T = I_o \frac{T^2}{(1-R)^2} \cdot \frac{1}{1 + F \sin^2\left(\frac{\Delta}{2}\right)}$$

In the expression above,  $I_T$  is the intensity as viewed from the transmitted side of the cavity,  $I_o$  is the initial intensity of the incoming beam, while  $T$ ,  $R$  and  $\Delta$  is as defined previously.  $F$  is the coefficient of finesse of the cavity, which will be further discussed shortly.

Since absorption is not considered in this ideal case, obtaining the intensity at the reflected side of the cavity can be done as shown below [38].

$$I_R = 1 - I_T$$

The intensity of the reflected side of the cavity is then shown by the following expression.

$$I_R = I_o \frac{T^2}{(1-R)^2} \cdot \left[ 1 - \frac{1}{1 + F \sin^2\left(\frac{\Delta}{2}\right)} \right]$$

In this equation,  $I_R$  is the intensity as measured from the reflected side of the cavity,  $I_o$  is the initial intensity of the incoming beam, and  $T$ ,  $R$  and  $\Delta$  is as defined previously.  $F$  is the coefficient of finesse of the cavity. Due to the design of the fiber based Fabry-Pérot cavity used in this project, the details of which are discussed in the next section, only the reflected intensity profile is measured during experiment.

The coefficient of finesse determines the shape of the fringes that are seen when observing the interference of the beams at either end of the cavity. The coefficient of finesse is defined by the following expression [38,43].

$$F = \frac{4R}{(1-R)^2}$$

As can be seen in the definition for the coefficient of finesse, reflectivity of the cavity is the only parameter that affects the sharpness of the fringes of the interference pattern.

The reflected intensity profiles for several different values of  $R$  are shown in Figure 10.

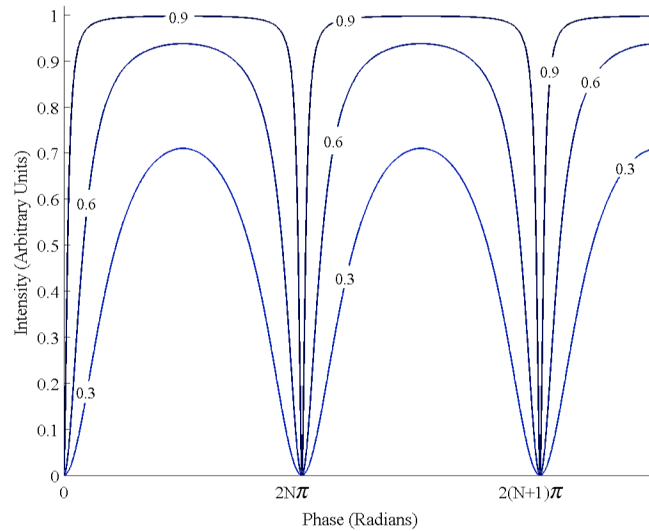


**Figure 10: Graph of the Reflected Airy Function for Different Values of Reflectivity ( $R$ ).** As can be seen in the figure, increasing the reflectivity of the cavity results in thinner fringes that, in turn, increase the performance of the cavity as a sensing device.

As can be seen in Figure 10, the trend is that as the reflectivity of the cavity is increased, the width of the fringes shrinks. Since many of the applications that a Fabry-Pérot is used for, including measuring distance, depend on measuring the position of the fringes, having a cavity with a high reflectivity is desirable. Methods of using a Fabry-Pérot cavity to measure displacement are shown in chapter 6 and in appendix 1.

For the case where the reflected system is measured, absorption characteristics of the cavity play an important roll [38]. Absorption can significantly reduce the measured intensity making the visibility of the fringes poor [45,46]. Hence it is important to note the reflectance, transmittance and absorptivity when selecting materials that will make up

a Fabry-Pérot cavity. Thin films of material can be deposited onto the faces of the cavity to improve the optical characteristics of the cavity. Optical properties of a material can vary with the wavelength of light that is used and with the thickness of the deposited material. The topic of thin films used for the fiber mirror that is attached to the thermal actuator is discussed in chapter 3.

### **2.3 Closing Remarks**

This chapter on the theory of the thermally actuated fiber based Fabry-Pérot interferometer provided an in-depth look into the workings of the chevron thermal actuator and the theory behind the Fabry-Pérot cavity. The section on thermal actuators showed many different approaches to modeling the complex thermo-mechanical system involved in the operation of a thermal actuator device. The Section covering thermal actuators also mentioned some of the important design parameters that affect the operation of the device. Most importantly, the effect of using temperature dependent expressions in any model was shown.

The section covering the theory behind the Fabry-Pérot cavity showed the derivation of the equations used to determine the fringe pattern resulting from light traversing the cavity. The Fabry-Pérot section also briefly mentions how the optical properties of the materials chosen for the cavity affect the performance of the cavity.

The proceeding chapter outlines in detail the design of the thermal actuator and the Fabry-Pérot cavity used in this project.

## **Chapter 3: Design of the Thermal Actuator and the Fiber Based Fabry-Pérot Cavity**

### **3.1 Introduction**

This chapter focuses on the design of the thermal actuator and the fiber based Fabry-Pérot cavity used in experiments for this project. As such, the chapter is split into a section dedicated to the design of the thermal actuator and another section on the design of the Fabry-Pérot cavity respectively. The section on the design of the thermal actuator covers additional features used to align the fibers of the Fabry-Pérot cavity to the actuator. The section on the design of the Fabry-Pérot cavity shows the thickness of materials used for the coated fiber mirror affect the optical properties of the cavity. The proceeding chapter outlines the fabrication of the thermal actuator and the cavity.

### **3.2 Design of the Thermal Actuator**

As has been previously stated, the type of thermal actuator used in this project is a chevron thermal actuator with a couple of additional features. The additional features used in this design are the backbone structure, which is where the input/output fiber is placed, and a trench that runs along the middle of the shuttle and backbone structure, which is used to align and mount the coated fiber mirror and the input/output fiber. Figure 11 shows a labeled depiction of the device used in this project. It is important to note that the sacrificial oxide in this depiction is exaggerated to show that the arms and shuttle are released from the oxide while the bond pads and backbone structure remain fixed to the sac-ox layer.



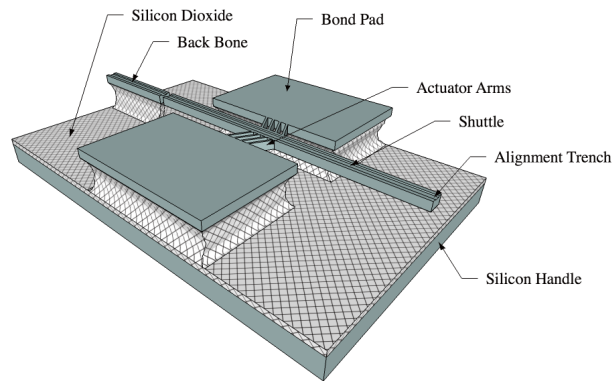


**Figure 11: Isotropic Depiction of the Thermal Actuator. The features that make up the device are the backbone structure, the bond pads, the actuator arms, the shuttle, and the alignment trench. The backbone structure holds the input/output fiber. The shuttle and trench hold the coated fiber mirror. The arms move the shuttle when they expand. Finally, the bond pads are where a voltage is applied to operate the device. Note that the thickness of the sacrificial layer is exaggerated for clarity. In the actual device, the sacrificial oxide is much thinner than the device silicon layer.**

It is useful to define each of the elements of the thermal actuator labeled in Figure 11.

The shuttle carries the fiber mirror and is attached to the arms of the thermal actuator.

The shuttle is 2910 microns long by 130 microns wide. A grid of 10 by 10 micron square holes are etched into the shuttle to aid in releasing the shuttle from the sacrificial oxide layer during the release etch. The actuator arms expand when current is passed through them causing the material to heat. Due to the initial bias angle of the actuator arms and the mechanical constraints of the device, the arms actuate the shuttle in the direction of the bias angle. The projected length, which is defined in chapter 3, is fixed at 195 microns. The length of the actuator arm is defined by the initial bias angle, which varies from one device to another on the wafer. The width of arms and number of pairs of arms also vary between devices on the wafer.

The actuator arms are anchored to the bond pads. The bond pads, as the name suggests, is where aluminum wire bonds are placed to power the actuator. The dimensions of the bond pad are 1520 microns by 1000 microns.

The backbone structure is where the input/output fiber is placed. The input/output fiber remains stationary while the thermal actuator moves the coated mirror. The backbone structure is located 50 microns from the back of the shuttle and is 130 microns wide by 1000 microns long.

The trench is used to aid in the alignment of the input/output fiber and the coated fiber mirror. The trench is etched 10 microns into the 20-micron device layer and is 64 microns at it's widest. Figure 12 shows a depiction of the cross section of the trench with a fiber placed in the trench.

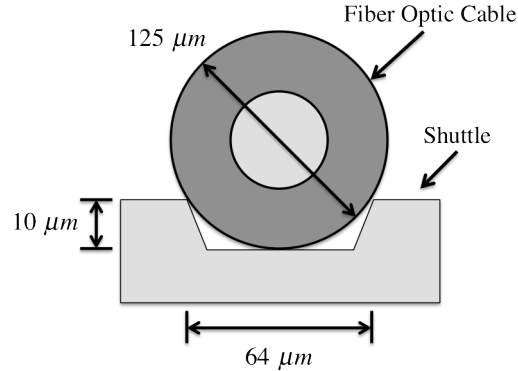


**Figure 12: Depiction of the Fiber Mirror Placed in the Trench on the Shuttle. The figure shows a cross-section of the shuttle. The trench is etched 10 microns into the device layer and is 64 micron at it's widest. The dimensions of the trench were chosen such that the fiber rests on the top edges of the trench.**

The dimension of the trench opening is calculated based on the requirement that a fiber 125 microns in diameter rests only on the topsides of the trench. An additional constraint on the trench dimensions is that the angle of the trench walls with respect to the vertical is fixed at  $54.7^\circ$  as a result of the anisotropic etch of silicon in KOH. The etch process used to create the trench is further discussed in the fabrication chapter.

As mentioned previously, some of the parameters of the thermal actuators vary across the wafer. The parameters that vary are the initial bias angle of the actuator arms, defined as  $\theta$  in chapter 2, the width of the actuator arms and the number of sets of arms per

device. Figure 13 shows a labeled drawing of the parameters that vary from one device to another on the mask design.

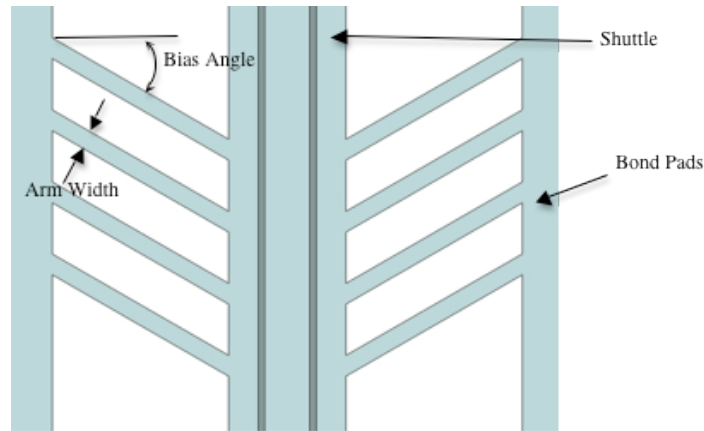


**Figure 13: Depiction of TA Parameters. The initial bias angle, the thickness of the beam and the number of arms vary from one device to another across the wafer.**

The mask design space varies the number of pairs of arms in two arm, four arm, and six arm configurations. The initial bias angle of the arms is spread from 5 degrees to 30 degrees in 5-degree increments, and the width of the arms varies as 3 microns, 5 microns, 10 microns, and 20 microns wide. Examples of the wide array of devices that occupy the design space are shown in Figure 14.

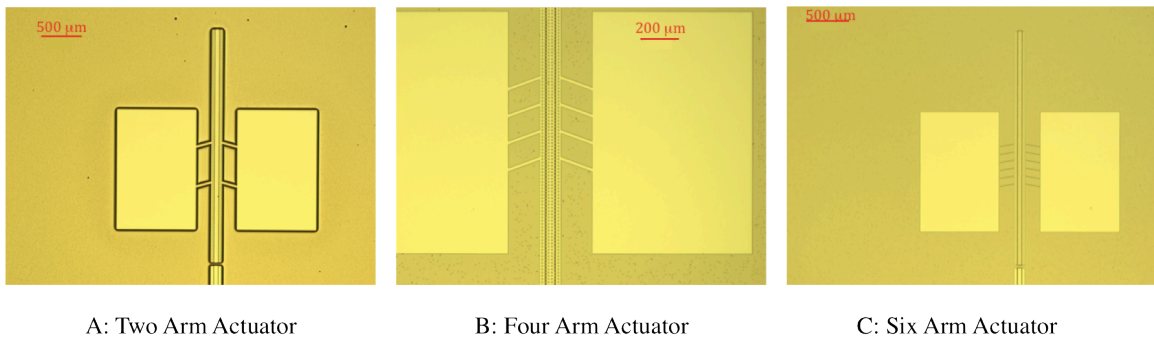


**Figure 14: Images of Different Thermal Actuator Designs that are Fabricated. Insert A shows an actuator with two sets of arms, insert B shows an example of an actuator with four sets of arms, and insert C shows an actuator with 6 arms. There are 72 different actuators on a given wafer. The device used in the experiments shown in this thesis has 6 pairs of arms that are 5 microns wide and have an initial bias of 5 degrees.**

By combining all possible design variations mentioned above, there are 72 different in total on a wafer. Unfortunately, due to time constraints, one device had to be chosen for

use in experiments for this project. The device chosen has six pair of arms that are five microns wide with an initial bias of five degrees.

Having discussed the design of the thermal actuators used in this project, the design of the fiber based Fabry-Pérot cavity can be reviewed in the proceeding section.

### **3.3 Design of the Fiber Based Fabry-Pérot Cavity**

The fiber based Fabry-Pérot cavity is made up of two flat-cleaved fibers. One fiber is designated as the input/output fiber and the other is titled the coated fiber mirror. No additional film coating is applied to the input/output fiber. The input/output fiber is placed onto the backbone structure and is used to input light into the cavity from a tunable laser and measure the reflected signal from the cavity. An experimental setup used to achieve this is further discussed in chapter 5. The coated fiber mirror consists of a coated scrap of fiber that is placed onto the shuttle with the aid of a probe and a Focused Ion Beam inside of a Scanning Electron Microscope (FIB, SEM respectively). The process of placing the both the coated fiber and the input/output fiber onto the actuator device are outlined in chapter 4.

As mentioned in chapter 2, the optical properties of the material of the mirrors that make up the cavity dictate the characteristics of the cavity. A depiction of the fiber based Fabry-Pérot cavity as viewed from the side is shown in Figure 15.

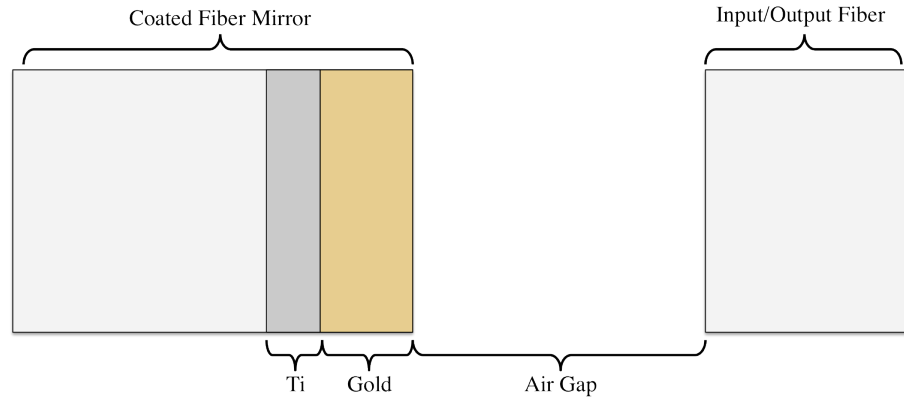


**Figure 15: Depiction of the Fabry-Pérot Cavity. Light enters from the right through the input/output fiber, which sits on the backbone structure, passes through the air gap, and encounters the coated fiber mirror. The fiber is located on the shuttle of the thermal actuator. The coated mirror is fabricated by depositing layers of titanium and gold onto a cleaved optical fiber via a CVD process.**

Proceeding from right to left in Figure 15, light travels through the input/output fiber, travels through the air gap and then encounters the coated fiber, which consists of a deposited 500-angstrom layer of gold that is adhered to the fiber mirror by 50 angstroms of deposited titanium.

As has been mentioned in chapter 2, the optical properties that affect the behavior of the cavity are the reflectivity, transmissivity, and absorptivity of the cavity mirrors. These properties depend on the type and thickness of the material used to coat the mirrors. The optical properties for a given film stack can be determined using the complex-matrix from of the Fresnel equations along with tabulated extinction and absorption coefficients [47]. Using a MATLAB script written by Dr. Zayd C. Leseman along with tabulated extinction and absorption coefficients for different wavelengths of incident light, one can model the reflectivity of the cavity mirrors vs. the wavelength of light incident on the cavity surface as well as the absorptivity, reflectivity and transmissivity of the cavity as a function of the film thicknesses. The tabulated extinction and absorption coefficients are taken from handbooks written on the optical properties of materials [48,49].

Figure 16 shows how the reflectivity of the coated fiber mirror varies as a function of the wavelength of light incident on the cavity (1495 nm to 1610 nm). The range of wavelengths used to create this graph match the range of wavelengths used in experiment.

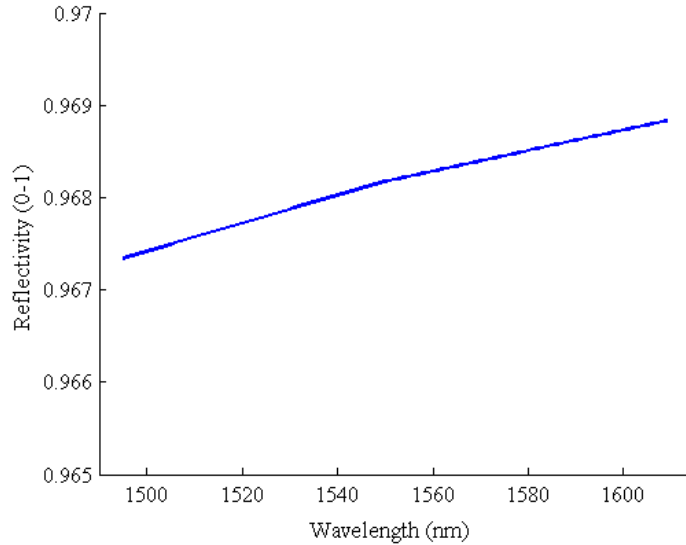


**Figure 16: Reflectivity of the Fiber Mirror as a Function of the Wavelength of Incident Light. The range of wavelengths shown match the range scanned using a tunable laser during experiments. The graph shows that gold exhibits excellent reflectivity across the bandwidth of light used in the experiments performed on the cavity in this thesis.**

As can be seen in Figure 16, gold has high reflectivity for the range of wavelengths used in the experiments performed in this project.

Figure 17 displays a graph showing how the absorbance, reflectivity, and transmittance vary with the thickness of the gold layer on the coated fiber. The thickness of the titanium layer remains a constant 5 nm. As mentioned before the titanium layer is only used to adhere the gold to the end of the cleaved fiber. Hence we only model how the thickness of the gold layer affects the optical properties. The wavelength of incident light on the cavity is fixed at 1550 nm.

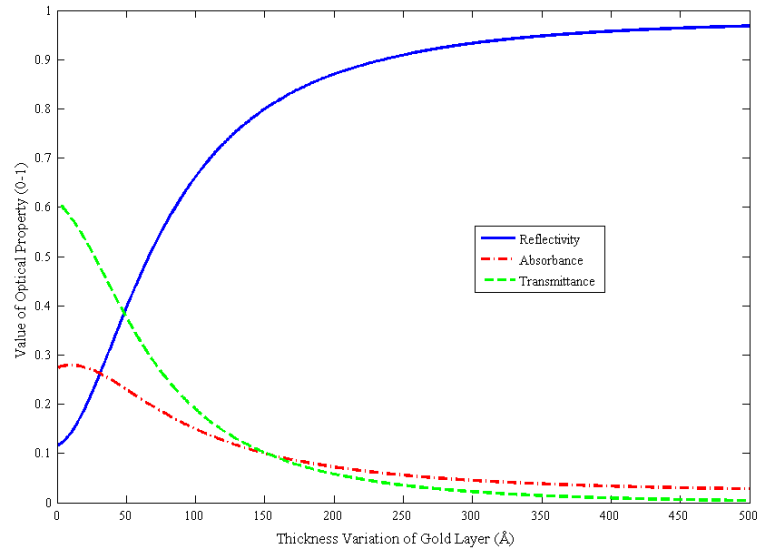


**Figure 17: Variation of Optical Properties with Respect to Au Film Thickness.** In this plot, the thickness of the gold film varies from 0 to 500 angstroms while the titanium layer is a fixed thickness of 5 nm. The wavelength of incident light on the mirror is fixed at 1550 nm. The graph shows that at 500 angstroms, the gold/titanium stack has excellent reflectivity, low transmittance, and absorbance. Since the signal is measured on the reflected side of the cavity, having low transmittance on the coated mirror is permissible. In future work, the code used to create this graph could be used in future work to optimize a coating for the input/output fiber.

As can be seen in Figure 17, a gold coating of 500 nm makes for a highly reflective, low absorbance and low transmissivity mirror. Since all of the measurements are taken from the input/output fiber, it is permissible to have the coated mirror have a low transmissivity. Using the same tools, however, one could tune the thickness of both the titanium adhesion layer and the gold layer to obtain a balance between the reflectivity, transmittance and absorbance and coat the input/output fiber as well. In future work, it would be advisable to coat both fiber mirrors to achieve a high quality cavity. Other recommendations for future work are shown in chapter 7, section 3.

### 3.4 Concluding Remarks

In this chapter, the details of the thermal actuator, along with additional structures such as the alignment trench and the backbone feature have been defined. The design space of

the various actuators that were patterned onto a wafer was also shown. Finally the critical dimensions of the actuator used with the Fabry-Pérot cavity in the experiments for this project was outlined. Additionally, how the thicknesses of the film materials affect the overall optical properties of the cavity was discussed in this chapter as well.

The next chapter shows the fabrication processes used to create the thermal actuators, to create and coat the fiber mirror, and how the fiber mirror and input/output fiber is placed onto the thermal actuator.

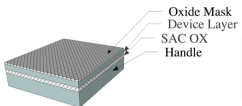
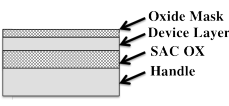
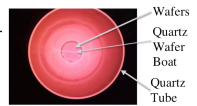
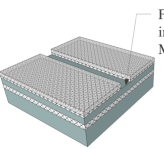
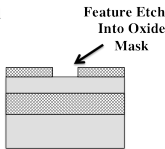
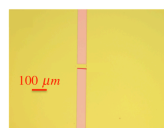
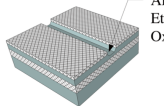
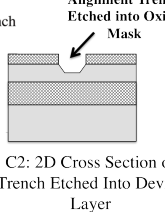
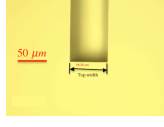
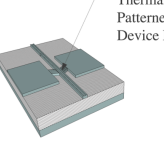
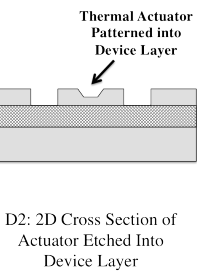
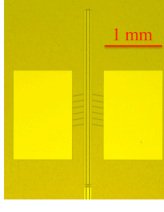
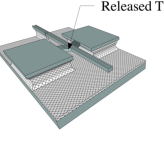
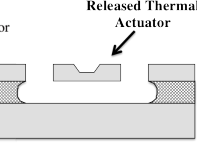
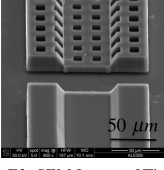


## **Chapter 4: Fabrication of the Thermal Actuator and Fabry-Pérot Cavity**

This section on fabricating the device is split into four parts. The first section describes fabrication of the thermal actuator device. The fabrication process of the fiber mirror is described in the second section. The third section describes a chip holder that is built to aid in placing the fiber mirrors, for transporting the device from the SEM to the laser lab, and to aid in testing the device in SEM and in the laser lab. The fourth section details the process of placing the fiber mirror onto the shuttle of the thermal actuator. The fourth section also describes placement of the input fiber onto the backbone structure of the actuator to complete the Fabry-Pérot cavity.

### **4.1 Fabrication of the Thermal Actuator**

The thermal actuator is created using common microfabrication techniques in the clean room facilities located at the MTTC complex at UNM. The base material for the devices is a 6" (150 mm) silicon on oxide (SOI) wafer consisting of a 600-micron thick handle of silicon, a 3-micron thick sacrificial oxide layer, and a 20-micron thick single-crystalline device layer. Three masking processes are involved in creating the thermal actuator. The three mask features to be patterned are as follows; alignment fork structures, shuttle trench structures, and finally the thermal actuator devices. A Process diagram of the primary steps required to fabricate the devices is shown in Figure 18.

Process Steps	3D Depictions of Process	2D Sections of Process	Images From Process	Description of Process
<b>Insert A: Oxide Grown on SOI</b>	 A1: 3D Depiction of SOI With Oxide	 A2: 2D Cross Section of SOI With Oxide	 A3: Wafers in Tube Furnace During Oxide Growth	A layer of oxide is grown on top of the SOI wafer. The oxide is used as a mask for the KOH etches to create the alignment forks and the alignment trench features.
<b>Insert B: Trench Pattern Transferred Through Oxide Mask</b>	 B1: 3D Depiction of Trench Pattern	 B2: 2D Cross Section of Trench Pattern	 B3: Alignment Trench Patterned in Photoresist	After using the alignment fork features to align the mask to the <110> direction, the trench is patterned and etched into the oxide.
<b>Insert C: Alignment Trench Etched In Device Layer</b>	 C1: 3D Depiction of Trench Etched Into Device Layer	 C2: 2D Cross Section of Trench Etched Into Device Layer	 C3: Image of Alignment Trench Etched Into Device Layer	The wafers are then etched in KOH to create the alignment trench features. After the alignment trenches have been patterned, the oxide mask is removed in a BOE bath.
<b>Insert D: Thermal Actuator Patterned Onto Device Layer</b>	 D1: 3D Depiction of Actuator Etched Into Device Layer	 D2: 2D Cross Section of Actuator Etched Into Device Layer	 D3: Image of Actuator Etched into Device Layer	The thermal actuators are patterned onto the SOI wafer. The pattern is transferred to the device layer using a DRIE process.
<b>Insert E: Thermal Actuator Released from SAC OX</b>	 E1: 3D Depiction of Released Thermal Actuator	 E2: 2D Cross Section of Released Thermal Actuator	 E3: SEM Image of The Released Trench and The Back Bone Structure.	The final step of the microfabrication Process is to release the thermal actuator from the sacrificial oxide (SAC OX). The actuator is released from the SAC OX by immersing the wafers in a BOE bath.

**Figure 18: Processing Steps for Fabricating Thermal Actuators.** The figure shows 3D depictions, 2D cross sections, and images from the main processing steps involved in creating the thermal actuators. Each main processing step is briefly described in the figure as well. In fabricating the actuators there are three masking processes involved. One mask is used to define the alignment mark features, another mask to device the alignment trench and a final masking process to define the thermal actuator.

The next three subsections describe how each of the features mentioned in the previous paragraph are made.

#### **4.1.1 Fabrication of the Alignment Forks**

The first features to be made are the alignment forks. Two sets of alignment forks are made on opposite ends of the wafer. Alignment forks are used to align the subsequent mask feature, the shuttle trenches, to the  $\langle 110 \rangle$  direction of the wafer. The mask is aligned to the  $\langle 110 \rangle$  direction of the wafer so that trenches can be created via an anisotropic etch of the device layer in Potassium Hydroxide (KOH) [50]. If the trench features are not aligned to the  $\langle 110 \rangle$  direction, the resulting trench will not be a trapezoidal shape. SOI wafer notches are insufficient to align to the  $\langle 110 \rangle$  direction alone because the lateral etch rate of  $\{111\}$  planes in KOH are very sensitive to angular misalignments. Etch rate of silicon in KOH increases by a factor of two for a misalignment of  $1^\circ$  which would complicate stopping the etch at a depth of 10 microns [51].

In preparation of patterning the alignment forks, a one-micron oxide mask is grown on the SOI wafer. An oxide mask is used instead of a photoresist mask because the etch rate of oxide in KOH is lower than that of a photoresist in KOH. KOH etches wet grown thermal oxide at 7.7 nm/min compared to over 17,900 nm/min for S1822 positive photoresist [52]. An oxide mask is made using a dry growth method in a tube furnace as show in insert A3 of Figure 18. The additional oxide layer is used as a mask for both the etching of alignment marks and etching of trenches into the device layer.

After growing the oxide mask, alignment fork features are patterned onto the wafers in photoresist. Part of the alignment fork patterned in photoresist is shown in Figure 19.

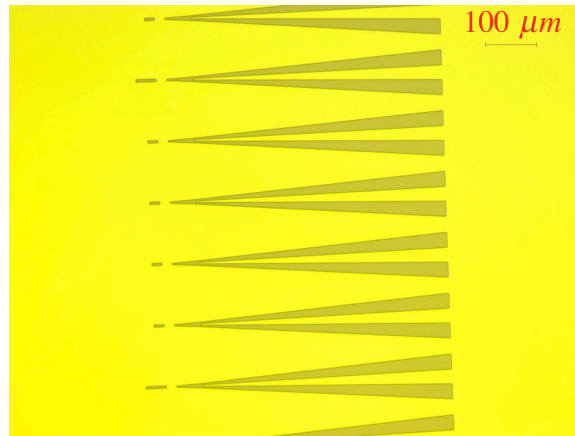


**Figure 19: Image of Alignment Forks Patterned in Photoresist (PR). The pattern is transferred through the oxide mask using a DRIE process after which the alignment forks are etched into the device layer using KOH. The alignment forks are used to align trench mask features to the  $\langle 110 \rangle$  direction of the wafer before patterning the trench features.**

The photoresist pattern is subsequently transferred to the oxide mask by etching the alignment fork pattern into the oxide using a DRIE process. The remaining photoresist is etched away in a piranha bath before performing the KOH etch to ensure the etch is uniform.

Once the alignment forks have been patterned into the oxide, the alignment fork pattern is etched into the device layer by submerging the wafer in a bath of KOH. The processes outlined above correspond to Inserts A through C in Figure 18.

#### **4.1.2 Fabrication of the Trenches**

The alignment fork pattern is used to align the wafer to  $\langle 110 \rangle$  direction so the trenches can be patterned. One can orient the mask to the  $\langle 110 \rangle$  direction of the wafer by observing which forks have been etched symmetrically. The mask is aligned to the forks which have the most symmetrical etch. Figure 20 shows an image of completed alignment marks.

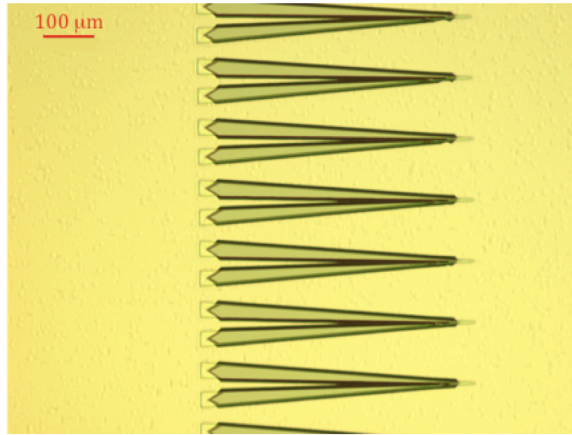


**Figure 20: Image of Completed Alignment Marks.** Note that the forks on the upper part of the image show asymmetry. The forks become more symmetric towards the bottom of the figure. The most symmetric forks on either side of the wafer are used to align the next mask to the  $\langle 110 \rangle$  direction of the wafer.

The alignment forks in the upper part of Figure 20 are asymmetric while the forks toward the bottom of the figure are more symmetric. After aligning the wafer to the mask, the trench features are patterned. An image of a trench feature patterned in photoresist is shown in Figure 21 and in insert B3 of Figure 18.

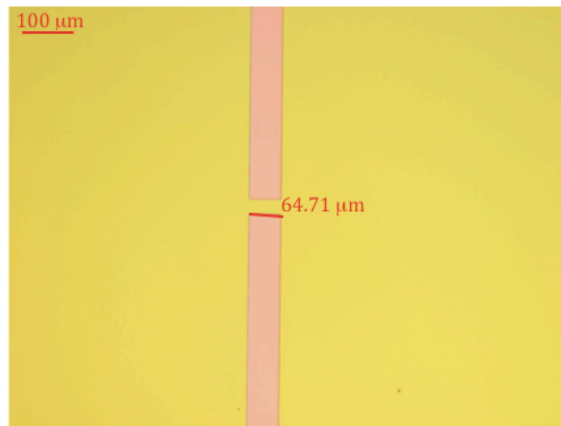


**Figure 21: Image of Trench Patterned in Photoresist.** After patterning, the trench is transferred to the device layer using a DRIE etch. The trench is then etched into the device layer via a KOH etch. The process step shown in this figure corresponds to insert B in figure 18.

The trench pattern is then transferred to the oxide mask using a DRIE process as shown in inserts B1 and B2 of Figure 18.

After transferring the trench features to the oxide mask and removing the photoresist mask in a piranha bath, the features can be etched into the device layer using KOH as

shown in insert C of Figure 18. Care must be taken during this etch to properly define the alignment trench. The depth of the trench is designed to be 10 microns. If the trench is under-etched, aligning the fibers into the trench will be difficult. Over etching the trench could result in a fragile shuttle or could even etch through the device layer completely.

To understand the parameters that affect the etch rate of silicon in KOH, the following empirical model by Seidel et al. is used [51].

$$R_{etch} = k_o [H_2O]^4 [KOH]^{1/4} e^{-E_a/k_b T}$$

In this equation,  $R_{etch}$  is the etch rate of silicon for a given crystalline direction in microns per hour,  $[H_2O]$  and  $[KOH]$  are the molarities of those respective substances,  $k_b$  is the Boltzmann constant,  $T$  is the temperature of the KOH bath in Kelvin, and both  $E_a$  and  $k_o$  are fitting parameters that are determined from experimental data. For a  $\langle 110 \rangle$  surface the fitting parameters are  $E_a = 0.60$  eV and  $k_o = 4500$  microns per hour [51].

From the empirical formula above, it is clear that the key tuning parameters for getting a constant etch rate are the bath temperature and the bath concentration. The upper limit on the temperature of the bath to obtain a maximum etch rate is around 80° C. The etch rate becomes non-uniform when the temperature of the bath is above 80° C [53].

To fabricate the trench features, the bath temperature is set to 80° C and the concentration of the bath is 45 wt%. The wafer is submerged in a KOH bath for 14 minutes to etch the trenches down to around 10 microns. A scout wafer used to test the fabrication process was sectioned in half to verify the etch process. An image of the sectioned wafer is shown in Figure 22.

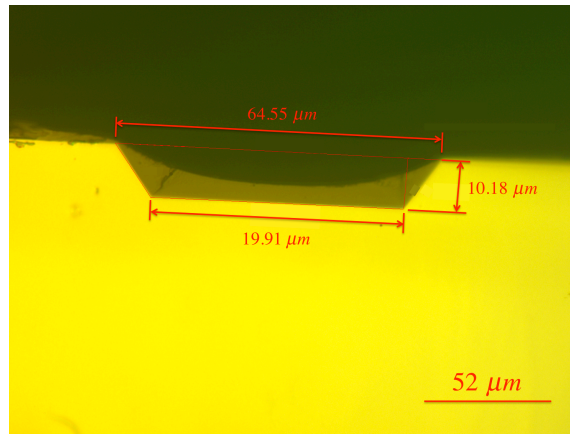


**Figure 22: Image of a Trench from a Sectioned Scout Wafer. The wafer was broke in half to obtain this image. As can be seen in the figure, the trench features are successfully etched into the silicon. The process step shown in this figure corresponds to insert C in figure 18.**

After etching the trench features, the oxide mask is removed by placing the wafer in a Buffered Oxide Etch (BOE) bath.

#### **4.1.3 Releasing the Structure from the Sacrificial Oxide**

The final feature fabricated on the wafer is the thermal actuator. The thermal actuators are first patterned in photoresist. Initially there were uniformity issues with coating the wafer with photoresist due to the trench features. The trench features caused the photoresist coating to be non-uniform after the spin coat process. The trenches caused the photoresist to fling out the trenches during the spin coat process, resulting in a non-uniform coating that is unsuitable for performing photolithography. Switching to a more viscous photoresist and by developing a new spin process alleviated the uniformity issue. Figure 23 shows an actuator patterned in photoresist.

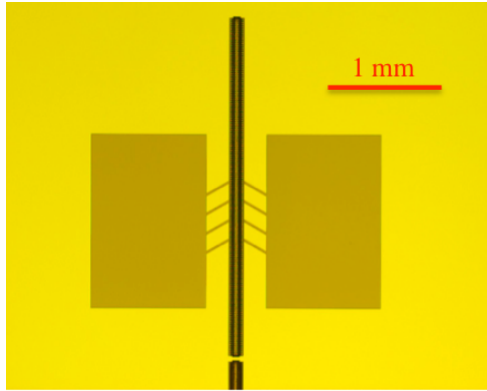


**Figure 23: Image of a Thermal Actuator Patterned in Photoresist.** The pattern is transferred to the device layer using a DRIE process. The process step shown in this figure corresponds to insert D in figure 18.

The pattern is then transferred through the device layer using a DRIE etch as shown in insert D3 of Figure 18. The photoresist mask is then removed using a piranha bath.

Piranha solution is a mixture of sulfuric acid and hydrogen peroxide that is used to clean organic residues, such as photoresist, off of a substrate.

The final fabrication step in making the thermal actuators is to release the shuttle and actuator arms from the oxide by etching the oxide in BOE as shown in the figures in insert E of Figure 18. The wafers are diced into individual devices and the dies are immersed in a BOE bath. Figure 24 shows an off-axis SEM image of the released device.

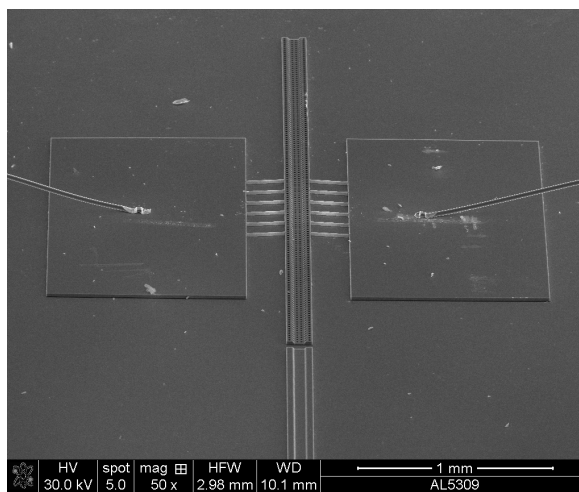


**Figure 24: SEM Image of Released Thermal Actuator.** The image was taken with the SEM stage tilted an angle. The aluminum wire bonds used to apply power to the actuator can be seen in the image. The process step shown in this figure corresponds to insert E in figure 18.



## 4.2 Description of the Chip Holder

In order to test the actuator inside a SEM and to facilitate moving the finished device with the Fabry-Pérot cavity attached, a chip holder is devised. The chip holder is made from plastic and is sized such that the holder can be mounted to a rotation stage in the SEM as well as an XYZ stage in the lab. A cleaved thermal actuator device is adhered to the center of the chip holder. Two strips of aluminum are also adhered to either side of the chip for use as external bond pads. The chip holder has two notches on the backside to facilitate placement of alligator clips onto the aluminum pads. An image of the chip holder is shown in Figure 25.

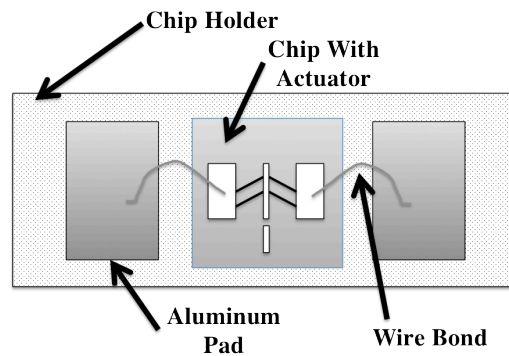


**Figure 25: A Depiction of the Chip Holder. The chip with the device is glued to the plastic holder. Aluminum bond pads are also adhered to the holder. Aluminum wire bonds connect the aluminum bond pads to the actuators bond pads. The chip holder is used to facilitate moving the finished device and for testing the device in SEM.**

A wire bond machine is used to connect the silicon bond pads of the thermal actuator to the aluminum bond pads on the chip holder. An SEM image of the wire bond on the silicon bond pad can be seen in Figure 26.

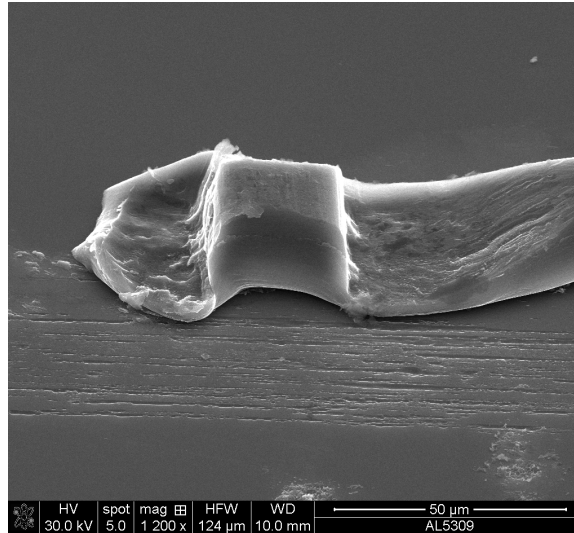


**Figure 26: SEM Image of an Aluminum Wire Bond on a Silicon Bond Pad.**

Aluminum is chosen for both the external bond pad and as the wire bond material because aluminum is easily bonded to itself and bonds well to silicon [54].

### **4.3 Fabrication of the Fiber Mirror**

As previously discussed, the Fabry-Pérot cavity consists of a gold-coated cleaved fiber attached to the shuttle structure of the actuator and an uncoated cleaved fiber connected to the backbone structure. The coated fiber consists of a flat cleaved optical fiber coated with a titanium adhesion layer followed by a gold layer using a chemical vapor deposition process (CVD). The fabrication of the gold-coated mirror is discussed in this section.

The first step in fabricating the gold-coated mirror is to cut sections of optical fiber into 3” strips. Next both ends of each strip are cleaved using a fiber cleave tool such that the ends of the fiber strips are flat. Each fiber strip is then bundled such that the ends of the fiber face the same side as shown in Figure 27.

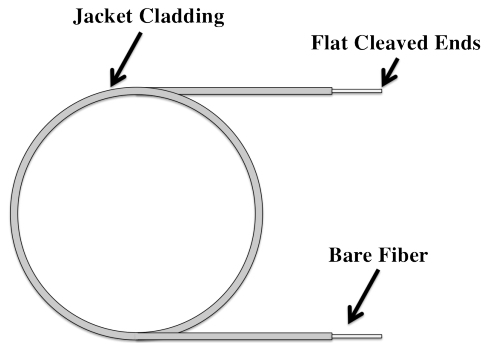


**Figure 27: Depiction of Bundled and Cleaved Fibers in Preparation for Coating the Fibers. The fibers are placed between two glass slides such that the flat cleaved ends are exposed to the CVD chamber. The glass slides and fibers are then placed into the CVD chamber where titanium and gold is deposited onto the surface of the fiber.**

The ends of the bundles are placed between microscope glass slides such that the end of each fiber is face down when mounted in the CVD chamber. Initially the fibers are coated with 50 angstrom of titanium as an adhesion layer to ensure that the gold adheres to the tips of the fibers. After depositing Ti, a 500-angstrom layer of gold is subsequently placed onto the tips of the fibers. The ends of the fibers are inspected using a microscope to check for damaged cleaves. An example of a good fiber end taken from a microscope is shown in Figure 28.

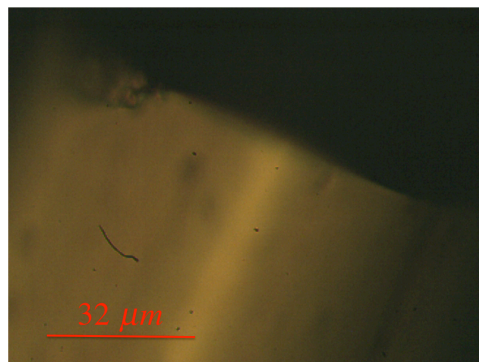


**Figure 28: Microscope Image of the Tip of Coated Fiber After CVD Processing. The optical fiber is flat cleaved then 50 angstrom of titanium is deposited onto the surface of the fiber as an adhesion layer. Afterwards, 500 angstrom of gold is deposited. The fiber is then cut down to a size where it can fit onto the shuttle of the thermal actuator.**

After the CVD process, the fibers which still have intact cleaves are further cut down into smaller segments so that they can be placed onto the shuttle of the thermal actuator.

## 4.4 Placement of the Fiber Mirrors onto the Thermal Actuator

This subsection details how the fiber mirrors are placed onto the device. The section is further split into two parts. One section focuses on placing the coated fiber onto the shuttle of the actuator and another section on placing the input/output fiber onto the backbone structure.

### 4.4.1 Placement of Gold Coated Fiber Mirror onto the Shuttle

The fiber mirror is placed onto the shuttle of the thermal actuator with the aid of a SEM FIB tool. To prevent charging effects from affecting the FIB tool and the SEM imaging, a bit of carbon paste is added to the gold-coated fiber.

To manipulate the fiber, the probe tip is attached to the carbon paste by depositing a block of platinum onto both the probe tip and the fiber. An image of the probe tip attached to the carbon paste on the fiber is shown in Figure 29.

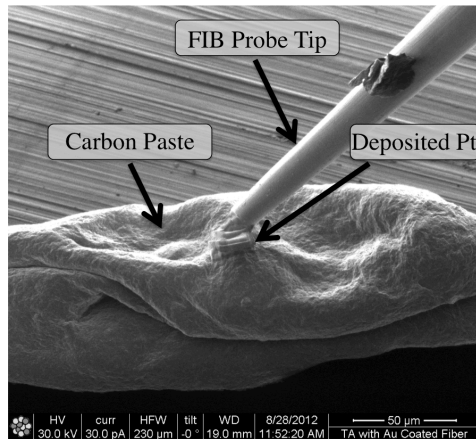


**Figure 29: SEM Image of the Probe Tip Attached to Carbon Paste. A bit of carbon paste is added to the top of the fiber mirror. The FIB probe is attached to the paste by depositing platinum onto the paste and the probe tool. The Probe tool is then used to place the fiber onto the shuttle of the actuator.**

The gold-coated fiber is then moved to the shuttle of the thermal actuator. To place the fiber into the trench, the fiber is first lowered into the trench and then one corner of the fiber is connected to the shuttle by depositing platinum onto both the fiber and the shuttle.

By constraining one corner of the fiber to the shuttle, the probe tip can be used to maneuver the fiber onto the trench.

Once the gold-coated fiber is in place in the trench, multiple depositions of platinum are placed between the trench and the fiber. The size of each deposition is 30x15x3 microns cubed deposited at 15 nA. It takes approximately 3 minutes to perform each deposition. Six depositions are done on each side of the fiber/trench interface. An off axis image of the deposits is shown in Figure 30.

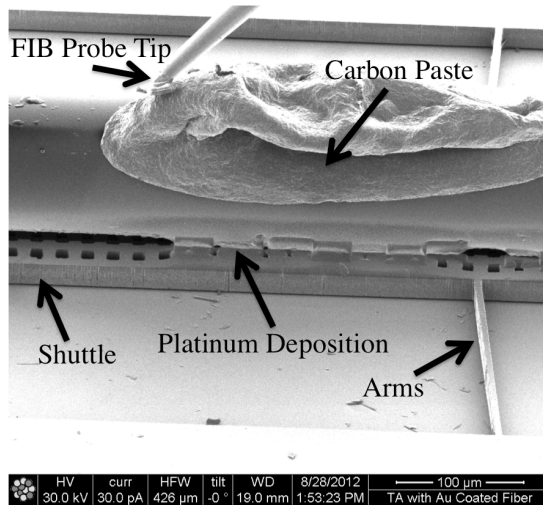


**Figure 30: SEM Image of Platinum Deposits on the Fiber and the Trench. The FIB tool is used to deposit platinum between the fiber and the trench. The FIB tool is then used to cut the probe tip from the carbon paste.**

Platinum is placed on both sides of the trench/fiber by rotating the SEM stage. The additional platinum depositions are necessary to ensure the fiber stays on the shuttle when transported to the lab for further testing. An off axis image of the attached gold-coated fiber is shown in Figure 31.

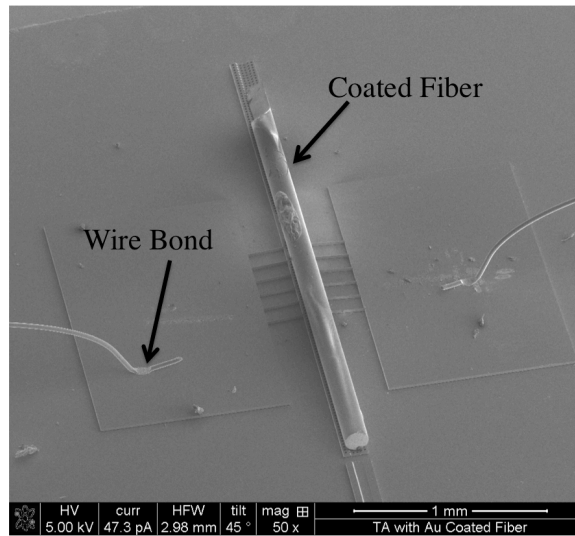


**Figure 31: SEM Image of a Gold-Coated Fiber Attached to Shuttle. The SEM image was taken with the stage tilted at an angle. The Insertion/Return fiber is placed onto the backbone structure using a separate setup outside of the SEM.**

The uncoated fiber is placed onto the backbone structure outside the SEM. The placement of the uncoated fiber is described in the next section.

#### **4.4.2 Placement of the Input/Output Fiber onto the Backbone Structure**

Placement of the input/output fiber is performed outside the SEM where the subsequent Fabry-Pérot experiments are executed. The fiber is bonded to the backbone structure using a UV-cured optical adhesive.

Since the backbone structure is located 50 microns away from the main structure, care must be used in applying the adhesive. The set-up used to bond the fiber to the backbone structure is as follows and is shown in Figure 32. The input/output fiber is placed onto the backbone structure with the aid of a microscope, a v-groove fiber holder attached to an XYZ stage for positioning the fiber, a rotational stage that the chip holder is placed on to align the backbone structure parallel with the fiber, and a probe tip manipulator tool to hold the input/output fiber in place during the bonding process. A second XYZ stage with a v-groove fiber holder along with a scrap fiber is used to apply the UV-cured optical

adhesive to bond the input/output fiber to the backbone structure. An illustration of the top view of the aforementioned set-up is shown in Figure 32.

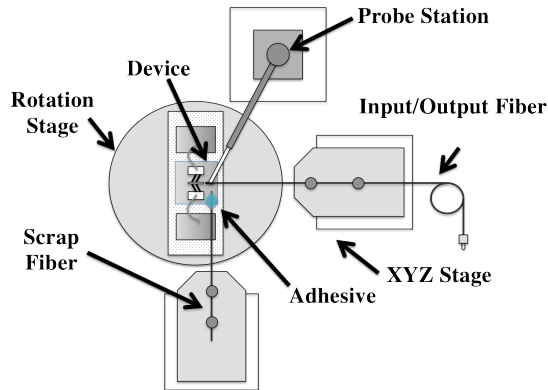


**Figure 32: Depiction of Fiber Bonding Setup for Placing an Input/Output Fiber on Device. The device is placed onto a rotation stage so that the backbone structure can be aligned to the input/output fiber. The input/output fiber is placed onto the backbone structure using an XYZ stage. A probe station is then used to hold the input/output fiber in place. UV cured adhesive is placed onto a scrap fiber to bond the input/output fiber to the backbone structure. Finally, the adhesive is cured using UV light.**

The procedure for bonding the input/output fiber is as follows. The fiber is flat cleaved and placed into the v-groove holder that is attached to the XYZ stage. Using the stage, the fiber is moved in place over the backbone structure. The chip is then rotated such that the trench on the backbone structure and the fiber are parallel to each other. Once the fiber is in place above the backbone structure, the fiber is lowered onto the structure using the XYZ stage. The probe tip is then lowered onto the top of the fiber to hold the fiber in place while adhesive is applied. To apply the adhesive to the insertion/return fiber, a drop of the adhesive is applied to a scrap piece of fiber. The scrap fiber is placed into the v-groove holder of the second XYZ stage and moved into position over the backbone structure. The scrap fiber carrying a drop of adhesive is then lowered down to the backbone structure until the drop covers both the input/output fiber and backbone structure, taking care to not let any of the adhesive cover the cleaved end of the insertion/return fiber or the probe tip. The scrap fiber is raised and moved out of the way.

A UV gun is used to cure the adhesive, bonding the insertion/return fiber to the backbone structure and thus completing the Fabry-Pérot cavity. The completed structure is shown in Figure 33.

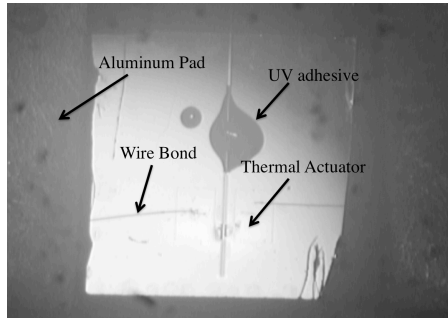


**Figure 33: Microscope Image of Completed Device. The Thermal actuator on the cleaved chip can be seen. The input/output fiber and the adhesive is also shown in the middle of the image.**

The tests of the Fabry-Pérot cavity are performed using this same mechanical setup along with additional data acquisition and optical equipment as is explained in the proceeding chapter.



## **Chapter 5: Experimental Setups and Testing Procedures**

This chapter covers the experimental setups and testing procedures used to evaluate the thermal actuator and fiber based Fabry-Pérot cavity. The chapter is split into two sections that cover experiments performed. One section describes the experiments performed on the thermal actuator in a Scanning Electron Microscope (SEM) before the coated fiber or input/output fiber is attached to the thermal actuator. The other section outline experiments performed in air after the coated fiber and input/output fiber are attached to the thermal actuator, creating the fiber based Fabry-Pérot cavity. In the SEM tests, the displacement is found via computer image analysis. In the in air experiments, displacement of the actuator is found by analyzing data obtained from the fiber based Fabry-Pérot cavity. The plots of resulting data are shown in chapter 7.

### **5.1 In-situ Testing of the Device in SEM**

In the first set of experiments performed, the thermal actuator is tested in an SEM. By using the SEM to image the thermal actuator during testing, it is possible to measure the displacement of the shuttle. The tests performed of the thermal actuator in the SEM are carried out before the coated fiber and the input/output fiber are placed onto the shuttle and backbone of the thermal actuator. Figure 34 shows a depiction of the experimental setup used for testing the thermal actuator in SEM.

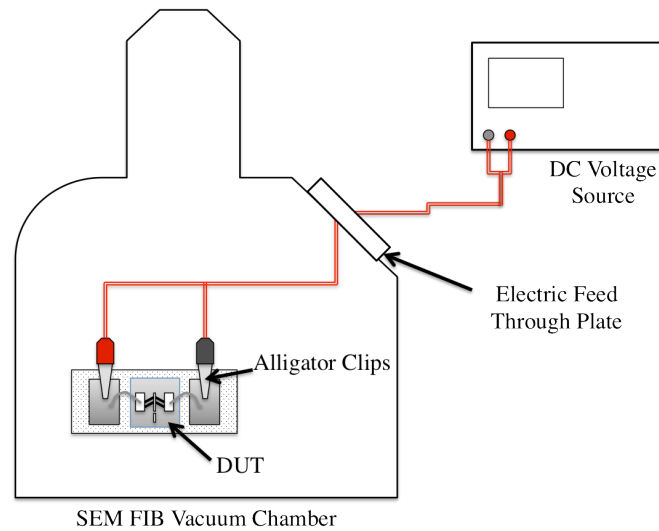


**Figure 34: Depiction of Experimental Setup for Tests Performed in SEM. The actuator is placed in the SEM and is connected to a DC power supply via the electric feed through plate.**

As is shown in Figure 34, the device, affixed to the testing platform described in chapter 4, is placed into the SEM chamber. Alligator clips are connected to the aluminum bond pads of the testing platform to provide power to the actuator. The other end of the cable is connected to an electric feed through plate on the chamber of the SEM. On the other end of the electrical feed through plate, a connection is made to a DC power supply that powers the thermal actuator during experiments.

Two tests are performed while the device is in the SEM; one where the rear of the shuttle is imaged as applied current is increased and another where the front of the shuttle is imaged as current is increased. The rear end of the shuttle refers to the end that faces the backbone structure and the front end is on the opposite side. The reason that the displacement at both ends of the shuttle is measured is due to the results of a multiphysics FEA model. The model, which is described in chapter 6, predicts that amount the shuttle heats during the test is significant. The resulting thermal expansion of the shuttle affects the overall displacement measurement at the front of the shuttle. Expansion of the shuttle will additively contribute to the displacement due to the expansion of the actuator arms.

At the rear of the shuttle, the expansion of the shuttle contributes to the displacement performed by the actuator arms in a subtractive manner.

Before applying current to the actuator, a reference line is cut into the substrate using the FIB so that displacement of the shuttle can be monitored during testing in the SEM. Rough estimates of displacement are found by measuring the distance from the shuttle to the reference line after each increase in applied current. The reference marks can be seen in the images in Figure 35 and Figure 36.

Each test starts with imaging the actuator before any current is applied. Current is slowly increased in 1 mA steps such that the actuator is in a state of thermal equilibrium. At each 1 mA current an image is taken of the actuator using the SEM. The current is increased in 1 mA increments until the rear end of the shuttle has moved approximately 1 micron as measured from the reference mark. Figure 35 shows three images of the rear of the shuttle taken at different applied currents.

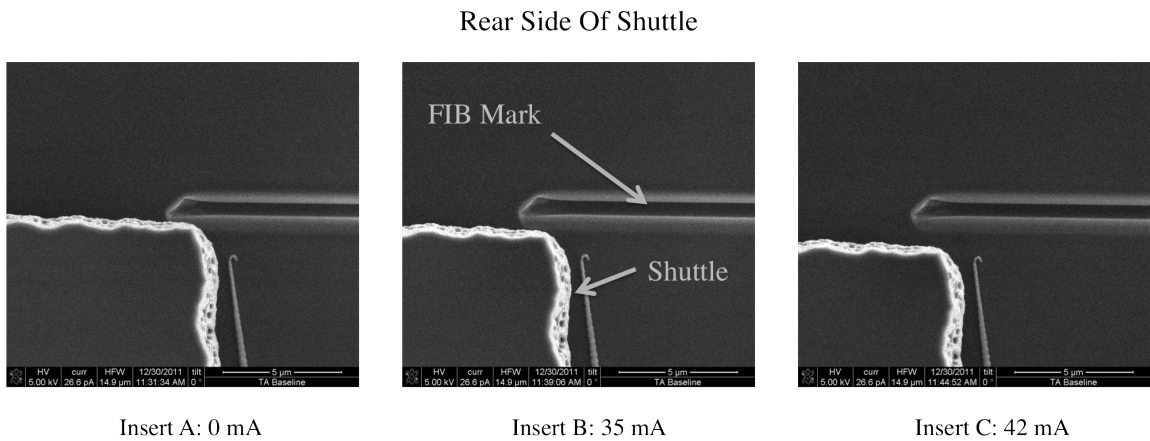


**Figure 35: SEM Images of the Rear of the Shuttle. The images show the shuttle moving as the current applied is increased. Insert A was taken with no applied current, insert B is with 35 mA applied, and insert C is taken when 42 mA is applied. In all of the images, part of the shuttle is shown along with a reference line that was drawn using the FIB into the substrate.**

Insert A in Figure 35 shows the rear of the actuator before current is applied, insert B is taken at 35 mA of applied current, and insert B shows the shuttle at a maximum of 42 mA of current applied to the actuator.

The above process is then repeated while imaging the front of the shuttle. Instead of increasing the current until the front of the shuttle has moved approximately 1 micron, the same range of currents used when imaging the rear of the shuttle, 0 mA to 42 mA are repeated. Figure 36 shows three SEM images of the front of the shuttle for different applied currents.

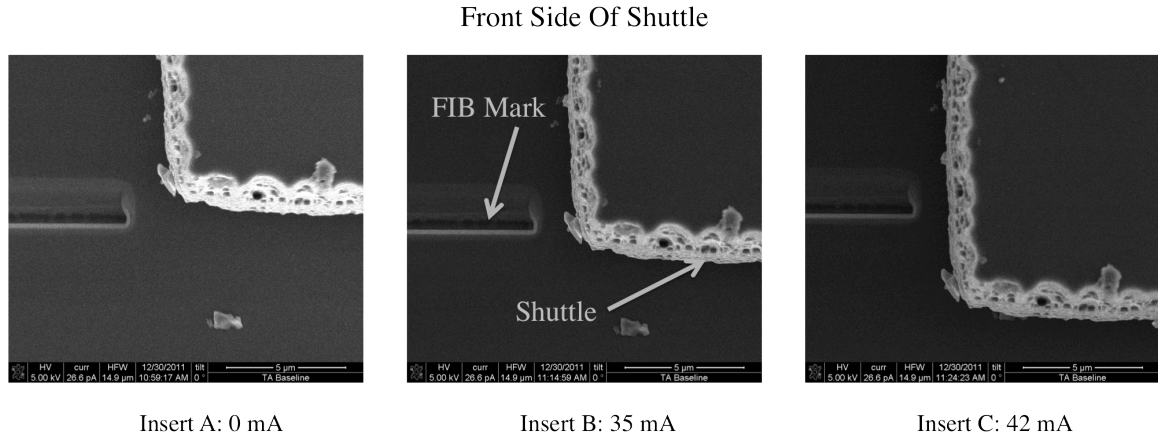


**Figure 36: SEM Images of the Front of the Shuttle.** Once again, the images show how the shuttle moves as the current applied is increased. Insert A is taken with no current applied. Insert B is taken when 35 mA is applied to the actuator and Insert C is taken when 42 mA of current is applied to the actuator. In comparing this figure to the previous figure, one can clearly see that the front of the shuttle displaces further than the rear of the shuttle due to heating and thermal expansion of the shuttle itself.

As in Figure 35, Insert A in Figure 36 shows the front of the shuttle with 0 mA applied to the thermal actuator, insert B shows the front of the shuttle with 35 mA applied to the actuator and insert C shows the front of the shuttle when 42 mA is applied to the thermal actuator. It should be noted that the same magnification is used when imaging both the rear and the front sides of the shuttle. By comparing the images shown in Figure 35 to those in shown Figure 36 one can clearly see the discrepancy in displacement due to the expansion of the shuttle as is predicted by the FEA model. The displacement of the front

end of the actuator is greater than the displacement of the rear end of the actuator over the same range of applied currents. Once again, the FEA modeling is one of the topics discussed in the next chapter.

SEM images taken during experiment are analyzed digitally using a MATLAB code written by Dr. Khawar Abbas to obtain accurate displacement data. The MATLAB image analysis code was originally written to measure the displacement of thermal actuators used as the basis of a nanoscale material testing apparatus [4]. The SEM images are collected at a horizontal field with of  $14.92 \mu\text{m}/\text{pixel}$ . Since it is generally accepted that for ridged body motion an accuracy of  $\pm \frac{1}{8}$  pixel can be achieved, a resolution of  $\pm 1.82 \text{ nm}$  is attainable using this method of measurement [4]. A displacement vs. applied current plot, as measured from the front side and rear side of the shuttle, is shown and compared to the FEA simulations in chapter 7, Figure 49.

After the SEM tests, the coated fiber mirror is attached to the shuttle using the SEM and the FIB tool as described in chapter 4. Later the input/output fiber is attached to the backbone structure using a UV curable adhesive, which is also described chapter 4. After completing the fiber based Fabry-Pérot cavity, experiments of the thermal actuator with the fiber Fabry-Pérot cavity are performed. These tests are discussed in the proceeding section.

## **5.2 Testing the Fiber Based Fabry-Pérot Cavity in Air**

Once the coated fiber and input/output fiber have been attached to the thermal actuator, experiments in which the Fabry-Pérot cavity is used to measure the displacement of the actuator can be performed.

The experimental setup used to test the actuator with the fiber based Fabry-Pérot cavity is depicted in Figure 37.

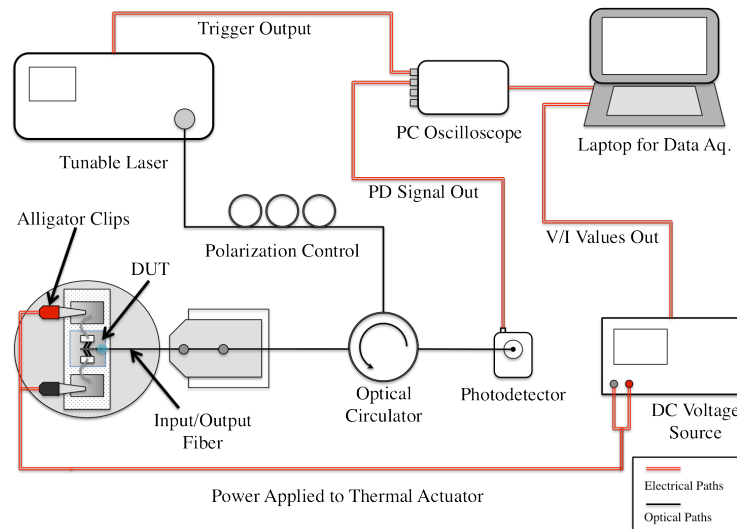


**Figure 37: Depiction of Experimental Setup Used to Test the Actuator in Air. A tunable laser is used to scan the cavity. The data acquisition system is triggered by the tunable laser to start data acquisition once a laser sweep is initiated. Using a fiber circulator, the light from the tunable laser is launched through the input/output fiber into the cavity. The reflected signal from the input/output fiber is feed into the circulator and sent to the photodetector. An oscilloscope is used to capture the signal from the photodetector.**

The tunable laser source is used to scan the cavity over the bandwidth of 1495 nm to 1610 nm. The output from the tunable laser is connected to a polarization controller and then sent to a fiber circulator. The circulator launches the light into the Fabry-Pérot cavity. The reflected light is then sent back into the circulator sending the light into a photodetector. The signal from the photodetector is measured using a PC-oscilloscope connected to a laptop. The trigger output from the tunable laser initiates data collection from the oscilloscope to start when a wavelength scan begins. The thermal actuator is powered by a DC power supply as shown in Figure 37. A long focal distance microscope is used to monitor the actuators movement during the experiment. Figure 38 shows an image of the shuttle with the coated fiber attached and the backbone structure with the input/output fiber attached.

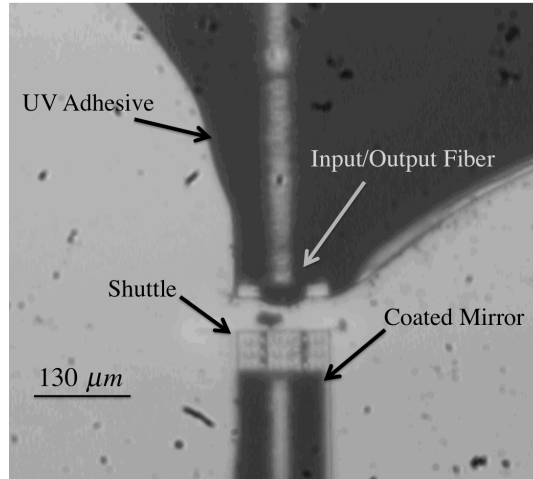


**Figure 38: Image of Fibers Attached to the Thermal Actuator. The coated mirror is attached to the shuttle and the input/output fiber is attached to the backbone structure.**

The procedure for experiments done in air on the thermal actuator with the cavity attached is as follows. At 0 mA an initial scan of the cavity is performed using the tunable laser. The current is then adjusted in 1 mA increments as was done in the tests performed on the actuator in SEM. At each increment, current and resistance readings on the DC power supply are recorded and a scan of the cavity is performed. The data from the cavity scan taken when no current is applied to the thermal actuator is shown in Figure 39.

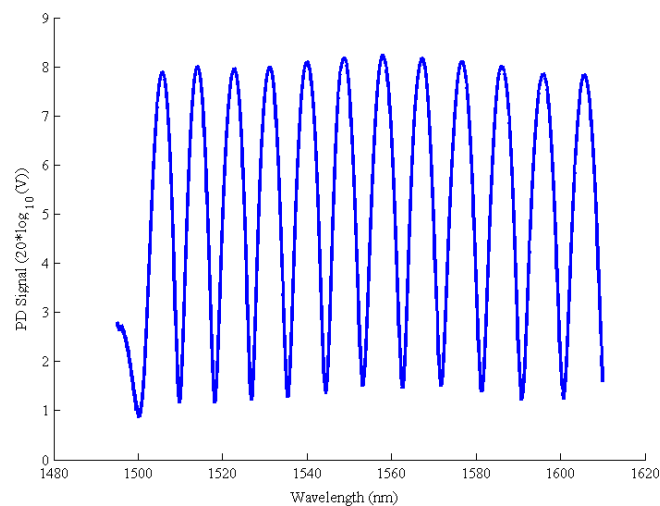


**Figure 39: Data of the Reflected Spectrum from the Fabry-Pérot Cavity. 0 mA is applied to the thermal actuator. The trace is obtained by scanning the laser from 1495 nm to 1610 nm.**

The range of currents applied to the actuator are 0 mA up to 100 mA. The range used for in air tests is higher than those used in SEM tests because of additional heat transfer by conduction to the air that occurs.

To obtain the displacement of the actuator, the wavelength scans of the Fabry-Pérot cavity are analyzed using a MATLAB code. The details of the how the MATLAB code computes the displacement is shown in the proceeding chapter.

The image analysis technique used in the SEM testing unfortunately could not be applied to in air experiments due to low magnification of the microscope used to monitor the experiments.

The next chapter details methods used to model the thermal actuator and the fiber based Fabry-Pérot cavity.



## Chapter 6: Modeling the Thermal Actuator and Fabry-Pérot Cavity

In this chapter, the methods used to model the behavior of the thermal actuator and the Fabry-Pérot cavity is discussed. The chapter is split into sections based on the topics to be discussed. In the first section, the FEA model used to simulate the behavior of the actuator is shown. The second section shows how displacement of the actuator can be determined by fitting data from the Fabry-Pérot cavity using a nonlinear least-squares tool written in MATLAB. Finally, the last section offers some concluding remarks for this chapter. In the next chapter, results from modeling outlined in this chapter are discussed.

### 6.1 Multiphysics FEA Modeling of the Thermal Actuator in Vacuum

A 3D FEA simulation is built using COMSOL multiphysics. The simulation utilizes a built in Joule heating and thermal expansion solver. The Joule heating and thermal expansion module numerically computes the temperature rise for a given current step applied to the actuator as well as the resulting thermal expansion of each element in the model. A full 3D simulation is run so that the affects out of plane motion is accounted for. Figure 40 shows the actuator geometry used in the simulation.

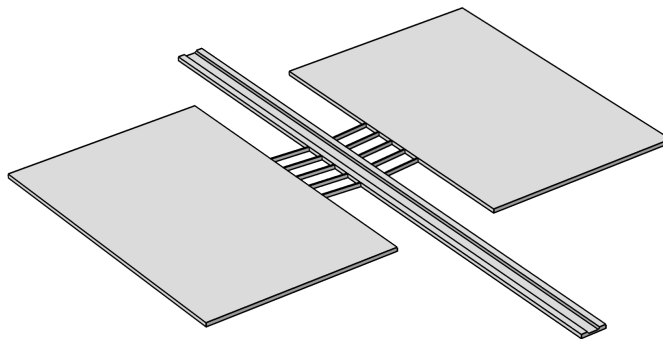


**Figure 40: 3D Geometry used in FEA Simulation. The alignment trench in the shuttle is taken into account in this model, however the etch holes in the shuttle are omitted due to memory constraints.**

Because this simulation is compared to the results from SEM experiments, heat transfer conducted from the actuator to the air is not considered, hence there is no domain modeled for air.

The 3D geometry is auto meshed using COMSOL's physics controlled meshing algorithm. The mesh is generated based on the physics modules used in the simulation and the constraints applied to the model. Figure 41 shows the mesh that applied to the 3D geometry.

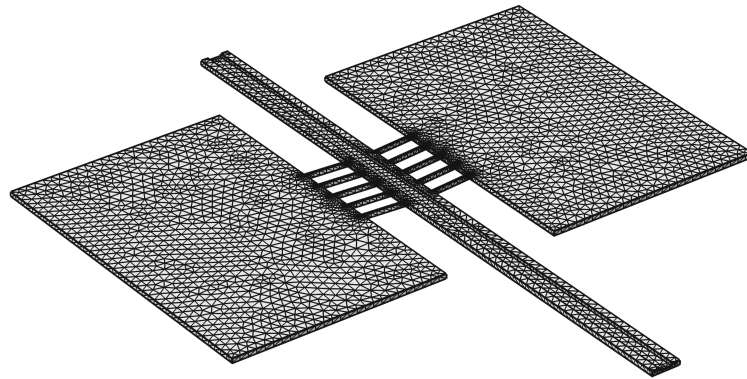


**Figure 41: Mesh used for the FEA Simulation. The mesh is created by COMSOL's physics controlled mesh based on the physics modules and constraints applied to the model.**

The proceeding sections discuss the boundary conditions used to create the simulation as well as the temperature dependent material properties used in the simulation.

### **6.1.1 Basic Conditions and Boundaries of the FEA Model**

The boundary conditions of the model are as follows. For the electrical part of the simulation, one bond pad is grounded while a floating potential is applied to the opposite bond pad. The current of the floating potential boundary is varied from 0 mA to 42 mA in 1 mA increments, matching the conditions of the experiment. The mechanical boundaries are that the bottom domains of the bond pads are fixed while all other domains are

unconstrained. The thermal boundaries are that Joule heating is applied to all of the domains of the simulation and that the initial temperature of the system is room temperature.

### 6.1.2 Temperature Dependent Materials Used in the FEA Model

As shown in chapter 2, using temperature dependent expressions for material properties can greatly improve the accuracy of the model. The materials that are assigned temperature dependent expressions in this simulation are the coefficient of thermal expansion (CTE),  $\alpha_{si}$ , the thermal conductivity,  $K_{si}$ , and the resistivity,  $\rho_{si}$  of single crystalline silicon.

The temperature dependent expression for the CTE of silicon used in the simulation is shown in the equation below from work done by Okada et al. [55].

$$\alpha_{si}(T) = \left( 3.725 \left\{ 1 - e^{-5.88 \times 10^{-3}(T-124)} \right\} + 5.548 \times 10^{-3} T \right) \times 10^{-6}$$

In this expression, T is the temperature of the actuator in kelvin. Other papers have also used Okada's work in their simulations [4,27,30].

The temperature dependent expression for thermal conductivity of silicon is a curve fit from experimental data found in the handbook "Properties of Crystalline silicon" by Hull et al. [56]. The curve fits were done by Torczynski et al. [57]. The expression used for thermal conductivity in the simulation is shown in the equation below.

$$K_{si}(T) = \frac{0.125 \times 10^4 + 0.165 \times 10^{-2} T^2 - 0.353 \times 10^{-5} T^3 + 0.241 \times 10^{-8} T^4}{1 + 0.13 \times 10^{-3} T^2 - 0.183 \times 10^{-6} T^3 + 0.109 \times 10^{-9} T^4}$$

Once again, the temperature of the actuator, T, is in Kelvin for this equation. The temperature dependent expression for the resistivity of silicon is also from a curve fit of

experimental data performed by Torczynski et al. [57]. The equation used in the simulation for the resistivity of silicon is shown in the equation below.

$$\rho_{si}(T) = 0.184 \times 10^{-3} - 0.307 \times 10^{-6}T + 0.627 \times 10^{-9}T^2$$

Once more, the temperature shown in the expression for the resistivity of silicon is in Kelvin.

Figure 42 shows graphs of the temperature dependent material properties.

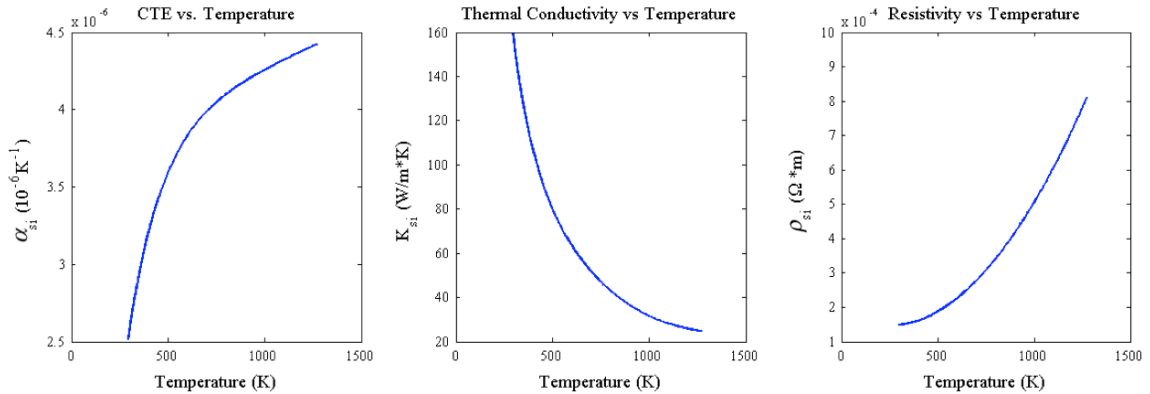


**Figure 42: Thermally Dependent Material Properties of Single Crystal Silicon. From left to right, the graphs are as follows. A.) Coefficient of Thermal Expansion of Si, B.) Thermal Conductivity of Si, and C.) The Resistivity of Silicon. The temperature range shown is from 294.15 K (21 °C) to 1273.15 K (800 °C).**

From left to right, Insert A in Figure 42 shows the CTE of silicon as a function of temperature, insert B shows the thermal conductivity of silicon and insert C shows the resistivity of silicon as a function of temperature. The temperature range used in generating these graphs is from room temperature of 294.15 K (21 °C) to the general maximum operating temperature of thermal actuators of 1273.15 K (800 °C).

### 6.1.3 Results of the FEA Simulation

As mentioned at the beginning of this section, the simulation uses a built in Joule heating and thermal expansion solver to determine the temperature, deformation and other parameters of a model for given applied currents. In this section, some of the results

from the simulation are shown. Figure 43 shows images of the temperature gradients of the actuator for different applied currents.

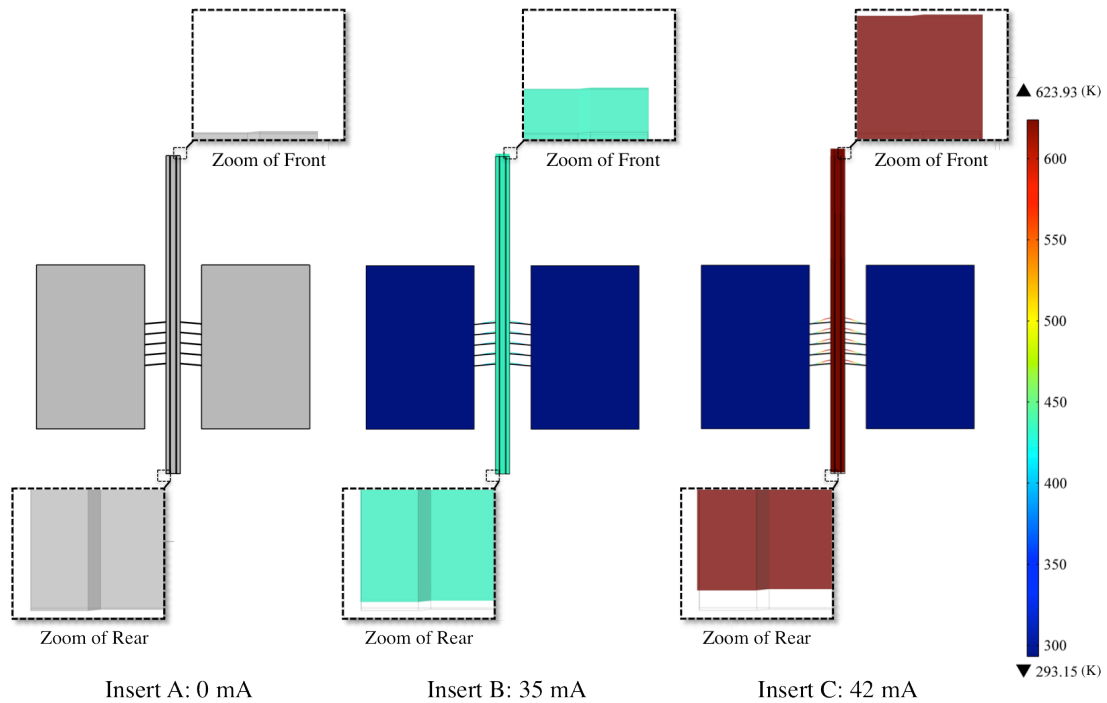


**Figure 43: Temperature Gradients and Deformation at Various Applied Currents.** Insert A shows 1 mA current applied to the TA. Insert B shows 35 mA current applied to the actuator and insert C shows the temperature distribution for 42 mA of applied current. The images also show how the actuator arms and shuttle expand with increasing current. The deformation scale is exaggerated by a factor of 15 for clarity.

Insert A in Figure 43 shows the temperature gradient at zero current, insert B is with a 35 mA current applied to the actuator and insert C shows the temperature gradient of the actuator with 42 mA of current applied to the actuator. The images in Figure 43 also show the deformation and displacement of the actuator. The original shape of the actuator is drawn in black outlines. Deformation in the overall actuator in the figure is exaggerated by a scaling factor of 15 for clarity. In the zoomed in areas of the figure, the scale is unity. Observing the zoomed inserts of Figure 43, one can see that the front of the shuttle shows a greater displacement than the rear of the shuttle due to the thermal expansion of the shuttle. The difference in displacement is due to the shuttle heating and

expanding as the arms move the shuttle. Expansion of the front of the shuttle contributes additively to displacement at the front of the actuator and in a subtractive manner at the rear of the actuator. Discrepancy in displacement of the front of the shuttle versus the rear of the shuttle from this simulation prompted the measurements of displacement at both sides of the actuator during experiments performed in SEM as noted in chapter 4.

Figure 44 depicts the temperature profile along the actuator arms and shuttle.

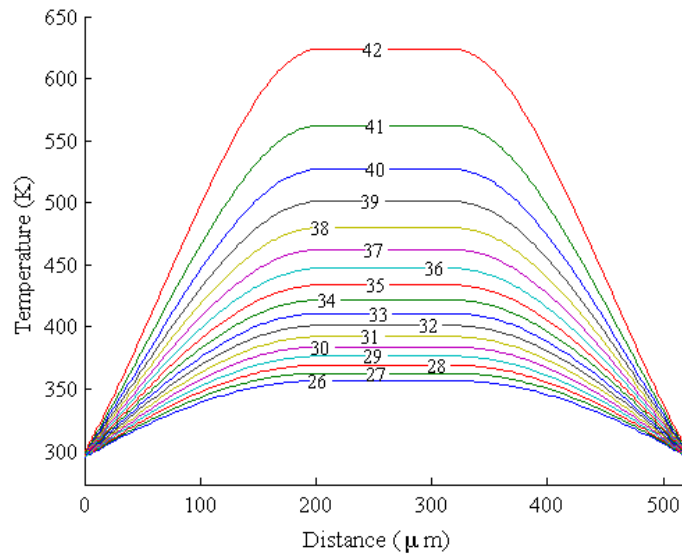


**Figure 44: Temperature Distribution Along the Legs and Shuttle of the Actuator. The maximum temperature is found along the shuttle. The ends of the actuator arms that are connected to the bond pads remain close to room temperature.**

As can be seen in Figure 44, the maximum temperature is found at the ends of the actuator arms connected to the shuttle and along the shuttle itself.

As mentioned in chapter 2, some papers ignored the shuttle in their model and hence the resulting graph are parabolas instead of the hump features shown in Figure 44 [29,31,32]. Simulations by Lott et al. show that for an actuator in vacuum, the shuttle temperature rises and becomes the highest temperature in the actuator. In air, however, heat transfer to the air lowers the temperature of the shuttle so that the maximum temperature is in the middle of the arms of the actuator [28]. Baker found similar results

using Raman spectra to measure the temperature of actuator arms experimentally [30]. Because of the lack of heat transfer to the air, an actuator in vacuum can reach peak temperatures with a lower input current than if the actuator operates in air [28]. The lowered shuttle temperature in air has the added benefit of reducing the amount of thermal expansion of the shuttle in the Fabry-Pérot tests.

Modeling the actuator in 3D allows for out of plane deformation of the shuttle to be observed. Figure 45 shows a graph of the shuttle, as viewed from the side, deforming out of plane as current applied to the actuator is increased.

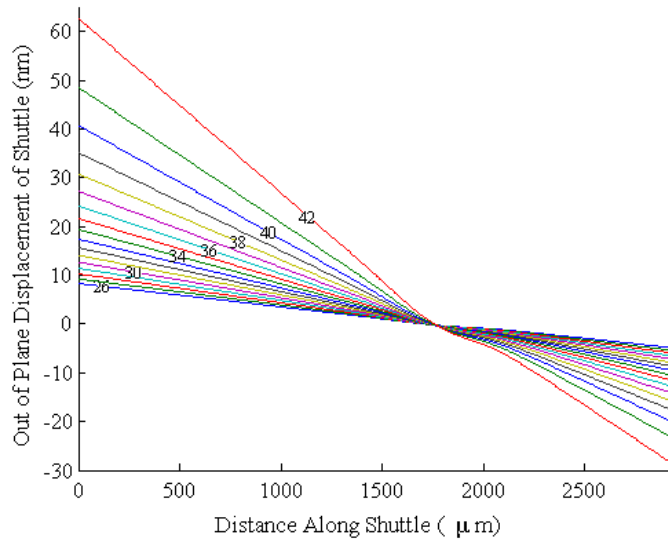


**Figure 45: Out of Plane Deformation of the Shuttle at Various Applied Currents.**

**The x-axis is oriented such that the front of the shuttle is at 0 microns. The y-axis shows the out of plane displacement. The shuttle is pivoted about the actuator arms.**

In Figure 45, the x-axis is oriented such that the front of the shuttle is at 0 microns. The graph shows that the shuttle pivots about the actuator arms. The front end of the shuttle is displaced approximately 60 nm above the plane and 30 nm below the plane. The out of plane displacement could adversely affect the alignment of the mirrors of the Fabry-Pérot cavity during operation.

The next section discusses the modeling of the data obtained from the Fabry-Pérot cavity during testing of the thermal actuator in air.

## **6.2 MATLAB Fitting of the Fiber Based Fabry-Pérot Cavity Data**

Two methods are used to determine displacement of the actuator from data taken from the Fabry-Pérot cavity. The first method discussed, titled the two-fringe method in this document, is used as an initial guess for the second method, titled the least-squares curve fit method. Each method computes cavity length at each current step. Recall from chapter 5 that scans of the cavity are taken at every 1 mA increase in current from 0 mA to 100 mA using the tunable laser. To determine displacement of the actuator, the cavity length computed at a given  $i^{\text{th}}$  current step is subtracted from the initial cavity length when 0 mA was applied to the actuator. Each method is explained in more detail in the subsequent sections below.

### **6.2.1 Two-Fringe Method of Obtaining Displacement of the Actuator**

The two-fringe method uses the spacing between the any two adjacent fringes, which is often referred to as the free spectral range (FSR), to estimate cavity length. The equation used to determine the cavity length is shown in the expression below.

$$d_{cav_i} = \frac{\lambda_1 \lambda_2}{2(\lambda_2 - \lambda_1)}$$

In this expression,  $d_{cav_i}$  is the cavity length at a given current step, while  $\lambda_1$  and  $\lambda_2$  refer to the wavelength of fringe 1 and fringe 2, which are adjacent to one another, respectively. The equation is derived from the airy function shown in chapter 2. As inferred by the equation, as the cavity length changes, the free spectral range of all adjacent fringes



change. This change can be used to determine the amount of displacement that occurs from one current increment to the next. The full derivation of this equation can be found in appendix 1.

A code was written in MATLAB to perform the two-fringe method of computing the cavity length for every pair of adjacent fringes in a given scan of the Fabry-Pérot cavity. The average of the all the cavity lengths computed from the fringe pairs is used as the cavity length for the given current step. Figure 46 shows a “check-plot” used while developing the MATLAB code. The plot shows that is code is able to find the location of the fringes in the data file.

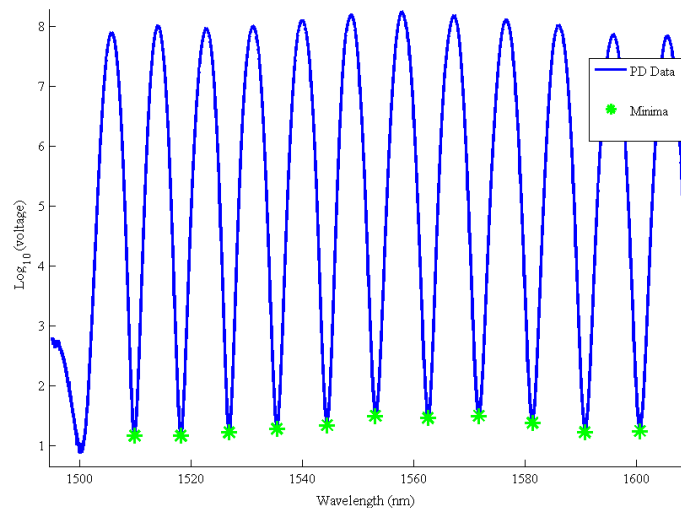


**Figure 46: Plot of MATLAB Code that Determines Minima of Fringes in a Given Data Set. The large green asterisks denote the location of the minima as determined by the MATLAB code.**

In Figure 46, the green asterisks show the location of the minimum of the fringes. Once again, the wavelength of the minima of any two adjacent fringes is used to compute the cavity length. The average value from all of the adjacent peaks is then used as the final cavity length estimation for the given scan. The reason the average cavity length is used is that, due to noise in the data, the local minimum for a given fringe might not be at the exact center of the fringe. Hence, the error using the two-fringe method to calculate

the cavity length can be high due to noise obscuring the true minimum of the fringes [40,41]. T. Wang et al. shows that for a reflectivity of 0.035 for a glass-air interface, the maximum error in the location of the fringe can be as high as 6.5% [39]. The two-fringe method can be augmented with a curve fitting method to improve the accuracy of the computation of the cavity lengths at each current step.

The next section shows the least-squares curve fitting method that is also used to compute the displacement of the actuator. The displacement versus current results of both methods is shown and discussed in the results chapter of this document.

### **6.2.2 Least-Squares Curve Fit to Determine Displacement of the Actuator**

The least-squares curve fitting method of determining displacement of the actuator utilizes a function in MATLAB's optimization toolbox for performing nonlinear least-squares curve-fitting of data. The function accepts a user defined equation and user defined coefficients that can be altered by the code until a best fit for the data is found. The user can define initial guesses for the coefficients as well as a range of values for the coefficients that the simulation can use to optimize the equation to the data. The equation used by the MATLAB code to fit the Fabry-Pérot cavity data is shown by the following expression.

$$I_{fit} = I_{est} \frac{1}{1 + F \sin^2\left(\frac{\Delta}{2}\right)}$$

In this expression,  $I_{fit}$  is the resulting intensity distribution found from the fitted function,  $I_{est}$  is the amplitude of the intensity distribution,  $F$  is the finesse and  $\Delta$  is defined as the following expression.

$$\Delta = \delta + \delta_R$$

In this expression,  $\delta_r$  is phase change to due reflection and  $\delta$  is defined by the following expression.

$$\delta = \frac{4\pi}{\lambda} d_{cav_i}$$

In the above expression,  $\lambda$  is the wavelength of light entering the cavity from the tunable laser source and  $d_{cav_i}$  is the cavity length at the given current step.

All of the coefficients, with the exception of  $\lambda$  and the constants, are to be optimized by the least-squares function in MATLAB. The initial guess for  $I_{est}$  is found by computing the average intensity of the data to be fitted. The bounds of the coefficients are chosen such that the curve fit function can only make small adjustments to the parameters.

The fitting function requires that the bounds of any parameter to be optimized to be tightly constrained [58]. Because the fitting function works best with tightly constrained boundaries on the coefficients to be optimized, this poses an issue for optimization of the cavity length parameter,  $d_{cav_i}$  and the finesse,  $F$  of the cavity. As previously mentioned, the initial guess for the cavity length comes from the average cavity length found using the two-fringe method. The boundaries for this parameter are set by the standard deviation of all of the cavities lengths found using the two-fringe method. The boundaries set by the standard deviation is larger than what the least-squares function requires to properly optimize the coefficients. Similarly, the boundaries of finesse are larger than what the least-squares function can accept to properly fit the equation to data.

A way of getting around the issue of needing small bounds on the cavity length and the finesse is to embed the least squares function in a for loop and step through smaller

increments within the overall boundaries that would otherwise be too broad for the least-squares fitting function. The next section describes how this method is implemented.

### **6.2.2.1 Procedure of Obtaining a Least-Squares Curve Fit to Data**

In order to tightly constrain the bounds of the cavity length and finesse coefficients two nests loops are used. The outermost loop iterates across possible cavity lengths while the innermost loop, which is where the fitting function is executed, iterates across possible finesse values. With every loop iteration of the inner and outer loops, a  $R^2$  goodness of fit is computed for the fitted function in comparison to the data.

The range that the outer loop steps through for the cavity guess is set by the standard deviation from the two fringe cavity estimates. The initial guess used is obtained by dividing the guess range by the number of desired loop iterations. The boundaries of displacements which the curve fit is able to use is also set by the number of iterations. As the number of loop iterations increases, the steps between loop iteration is finer at the cost of increased computing time. As an example, within the inner for loop the finesse varies from 0.5 to 1.2. The initial guess for the finesse for a given iteration within the loop is set by the dividing the guess range by the number of iterations along with what the current iteration of the loop is.

As mentioned earlier, the curve fit operation is performed within the inner loop. The  $R^2$  value of the curve fit to the data is performed during every loop iteration as well.  $R^2$  values along with the corresponding coefficients are collected as the code runs.

Figure 47 shows a contour plot of how  $R^2$  values of the curve fits vary for the combinations of cavity length and finesses coefficients of the curve fit function operating

on a single data trace. The figure is made from the optimization code output from the data scan of the Fabry-Pérot cavity at 0 mA of current applied to the actuator.

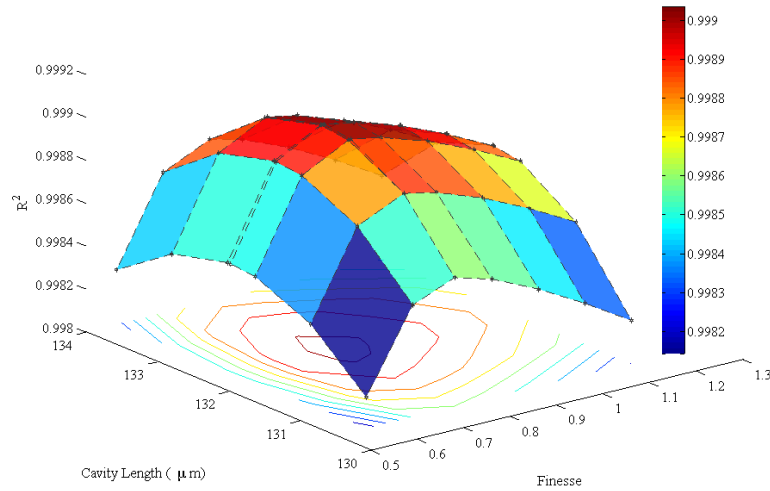


**Figure 47: Plot of  $R^2$  Values of Curve Fits as Cavity Length and Cavity Finesse Value Vary. The graph above is created from the  $R^2$  goodness of fit values of various curve fits to the FP data. The cavity length from the combination that yields the highest  $R^2$  value is then used to find the displacement of the actuator for the given current step. The graph shown is for 0 mA current applied to the actuator. Once again, this process is repeated for every data set from 0 mA to 100 mA current applied to the TA.**

In Figure 47, the x-axis shows the cavity length as optimized by the curve fit and the y-axis shows the finesse as optimized by the curve fit. The z-axis shows how the  $R^2$  value of the curve fit corresponds to pairs of cavity length and finesse values. The cavity length associated with the coefficient set that yields the overall highest  $R^2$  value is taken to be the cavity length for the current step corresponding to the given cavity data.

Figure 48 shows the curve fit corresponding to the highest  $R^2$  value plotted with the data for the scan of the Fabry-Pérot cavity when zero current is applied to the thermal actuator.

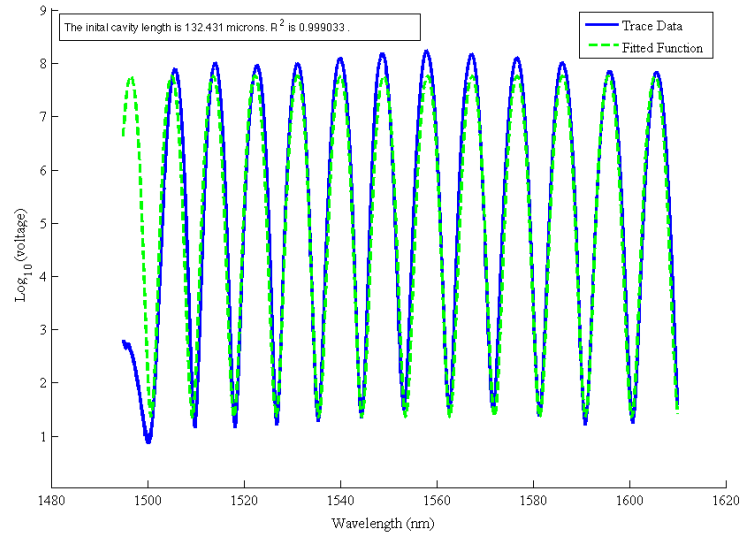


**Figure 48: Equation Best-Fit Plotted Along With Data at 0 mA. The fitted equation shown uses the coefficients that yield the highest  $R^2$  value as shown in Figure 47. The process of finding the best fit to obtain the cavity length at each current step is repeated for each data trace that was obtained. Data sets were taken for every 1 mA increase in current up to 100 mA. The displacement of the cavity is computed by subtracting the cavity length found at a given current step from the initial cavity length.**

As shown in Figure 48, the optimized curve fit closely matches that of the data.

The entire processes of determining the best curve fit is repeated for all of the data scans of the Fabry-Pérot cavity that were taken, from 0 mA to 100 mA, to find the length of the cavity at each current step.

As mentioned before, displacement of the actuator is then computed by subtracting the cavity length at a given current step from the baseline cavity length when no current is applied to the thermal actuator.

The resulting graphs of current versus displacement as determined by both the two-fringe method and the curve fitting method are shown in the next chapter.

### 6.3 Concluding Statements

To conclude, this chapter has shown methods used to compute displacement of the thermal actuator for each of the experiments that were performed on the device. To verify

the results from the experiments performed in SEM, a multiphysics model was created. To show how the displacement of the thermal actuator can be monitored using a fiber based Fabry-Pérot cavity, two complimentary methods of analyzing the data from the Fabry-Pérot cavity were implemented; The two-fringe method and the least-squares curve fit method.

The next chapter shows the displacement versus applied current results from these simulations in comparison to the data collected during experiments.

## **Chapter 7: Results and Discussion**

In this chapter, the results of the experiments and modeling are discussed. The chapter is split into sections according to experiments performed along with a section on improvements that could be made. The first section is on tests performed on the thermal actuator in SEM and the FEA simulation based on those experiments. In the second section, results of from experiments performed on the thermal actuator with the fiber based Fabry-Pérot cavity is shown. Finally, the third section outlines issues encountered with the design of the thermal actuator and of the experiments and offers suggestions of improvements that could be made in future work.

### **7.1 Tests Performed on the Thermal Actuator in SEM in Vacuum**

Recall from chapter 5 that the thermal actuator was placed into an SEM and actuated while inside the SEM. Displacement versus current data was taken for both the front side and rear side of the actuator. While imaging the rear side of the shuttle, the current source was increased from 0 mA in 1 mA increments until the shuttle moved around 1 micron. The front end of the shuttle was then imaged while the same range of currents was applied to the actuator. Using images taken during the experiment, a MATLAB image analysis code computed the displacement of the shuttle [4].

A multiphysics FEA simulation with temperature dependent material properties is used to model the thermal actuator in a vacuum environment. Displacement versus current data from the SEM imaging and from the multiphysics simulation is shown in Figure 49.



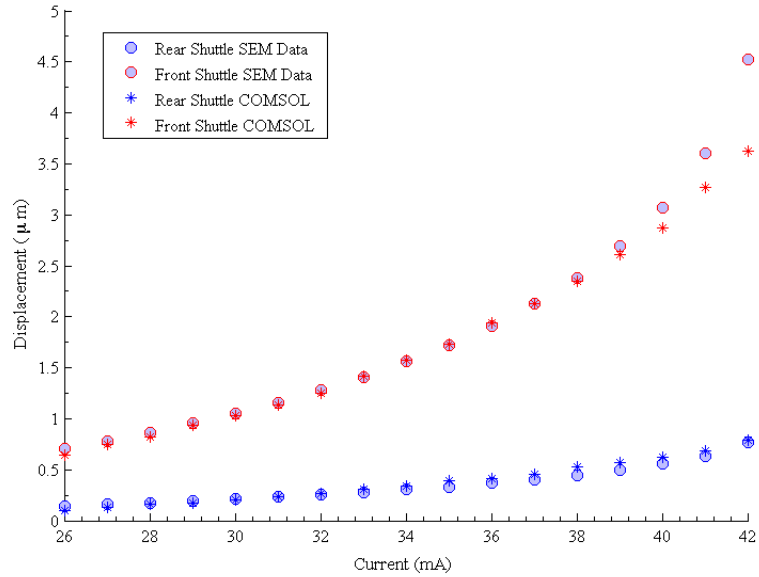


**Figure 49: Displacement of Front/Rear of Shuttle vs. Applied Current of SEM Data & FEA. The displacement from the SEM imagery and the displacement found from FEA are shown. The results from the FEA model closely match that of the data from the SEM experiments. It is important to note that the experiments performed in the SEM were in a vacuum environment.**

As shown in Figure 49, FEA simulation results match well with experimental data.

Experimental data and FEA simulation results demonstrate that the heating of the shuttle is not negligible. Expansion of the shuttle affects the displacement, as measured from the front of the shuttle, in an additive manner and affects the displacement, as measured from the rear of the shuttle, in a subtractive manner.

For applications such as nanomaterial testing, expansion of the shuttle adversely affecting displacement measurements is unacceptable. While this affect could be smaller in air, it could still affect measurements taken with the Fabry-Pérot cavity as well.

Some methods of mitigating the issue of the shuttle heating are discussed in the third section of this chapter.

## 7.2 Tests Performed on the Thermal Actuator in Air

As shown in chapter 5, a tunable laser scans the cavity and a photodetector is used to measure the reflected signal from the cavity. Scans of the cavity are taken at every 1 mA increase of current applied to the thermal actuator from 0 mA up to 100 mA.

Unfortunately the MATLAB image analysis that was done with the SEM imaging could not be done in these experiments due to the low magnification and low resolution of the camera used to monitor the actuator during tests.

To obtain displacement of the actuator using the Fabry-Pérot cavity, two complimentary methods are used. One method is the two-fringe method in which the wavelength of the minima of two adjacent fringes is used to estimate the length of the Fabry-Pérot cavity. The other method is to perform a least-squares fit on the data using the cavity length from the two-fringe method as an initial guess for the fit. Displacement is found by subtracting the cavity length found at a given current input from the length of the cavity before current is applied to the thermal actuator. The displacement versus current data obtained from the Fabry-Pérot data using the two different methods is shown in Figure 50.

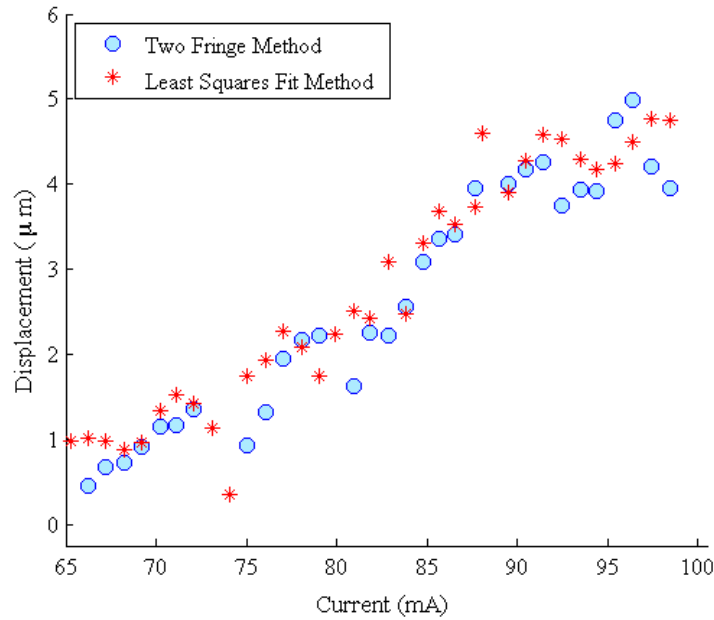


**Figure 50: Displacement vs. Current Plot Derived from Fabry-Pérot Cavity Data.** The figure shows data from the two-fringe method and the least squares curve fit method. The experiments of the Fabry-Pérot cavity were performed in air and hence higher current was applied to the actuator than in the SEM tests.

From Figure 50, it can be seen that the two-fringe method and the least-squares curve fit method both yield results that are of poor resolution in comparison to the SEM imaging method. The general trend and maximum values of the current versus displacement data seems reasonable despite the spread.

Some possible explanations for poor resolution seen with displacement derived from the Fabry-Pérot cavity measurements are as follows. The two-fringe method of calculating displacement, as was discussed in the modeling section, is fairly low resolution. Some alternative methods of finding the displacement are discussed in the next section of this chapter. There could also be alignment issues with the fiber mirrors despite the implementation of the alignment trench built into the thermal actuator device. Possible sources of misalignment include thermal expansion of the actuator causing misalignment of the coated mirror with respect to the input/output fiber as shown in Figure 45. Another source of out of plane deformation could be that the shuttle is initially

non-planar due to built-in stress being relieved when the shuttle structure was released from the oxide during fabrication. Methods of mitigating alimented issues, as well as improvements to the experiment are discussed in the next section.

### **7.3 Future Improvements to Device and Experiment**

In this section, the issues outlined above are addressed and possible solutions to those issues are proposed.

The two-fringe and curve fitting methods as implemented in this thesis are not adequate for precisely determining the position of the thermal actuator from data taken from the Fabry-Pérot cavity. There could be also be a misalignment of the coated mirror with respect to the input/output fiber due to out-of-plane thermal expansion of the shuttle. Recall that the input/output fiber is mounted to a stationary structure, called the backbone structure, which is not heated during the experiments. The shuttle heats and expands out of plane while the backbone structure holding the other mirror does not. Additionally, there could also be misalignment of the mirrors if the shuttle is not perfectly in plane. The shuttle could be slightly curved due to the release of built in stress in the device layer during the release stage of the device. This curvature would only get worse as the shuttle heats and expands during operation. An additional issue, mentioned in chapter 2, is that at high temperatures, an oxide layer can form on the actuator material.

Work required to improve analyzing data from the Fabry-Pérot cavity, improvements to mitigate the misalignment issue between the fiber mirrors, as well as design changes to prevent the central shuttle from expanding and heating, and a potential solution to the

actuator material oxidizing during high temperature operation are outlined in the following paragraphs.

A different method of measuring the displacement of the cavity is by creating a quadrature signal that is, by definition,  $90^\circ$  out of phase with the reflected signal using a second reference cavity [40] or by electronic methods [39,42]. Seat et al. were able to achieve a resolution of 40 nm and Wang et al. were able to achieve a resolution of 0.005 nm in a fiber based Fabry-Pérot cavity using these methods [39,42].

As mentioned before, the parallel-plane mirrors that make up the cavity are quite sensitive to misalignment. One way to reduce the misalignment issue is to switch to different cavity mirror geometries that are inherently less sensitive to misalignment errors than the plane-parallel plate cavity. An example of a cavity that is less sensitive to misalignment is a hemispherical cavity. Hunger et al. created approximately hemispherical cavities on cleaved fibers using a  $\text{CO}_2$  laser source to machine the fiber [13]. An additional benefit of switching to this geometry is that it is also possible to achieve high finesse cavities. In the same work, Hunger et al. reported a finesse of over 130,000 [13].

To minimize the possibility of the shuttle not being planar, an additional tensile film could be deposited atop the thermal actuator before the device is released from the substrate. Using common values for film stresses, an FEA simulation could be created to tune the thickness of the film needed to flatten the shuttle structure. Potential issues of a coefficient of thermal expansion mismatch between the deposited film and the actuator material leading to undesired behavior during the operation of the actuator would also be investigated using FEA models.

As shown in chapter 6 and 7, the heating and resulting thermal expansion of the shuttle adversely affects the displacement measurements of the device. One method of reducing the heating of the shuttle is to add heat sink structures to the shuttle structure. Zhu et al. utilizes heat sink structures in their thermal actuator based nanomaterial-testing device. Zhu et al. found that by using six pairs of heat sink beams the maximum temperature increase near the critical part of the shuttle was reduced from 300 °C down to 200 °C. Additionally, the heat sink beams also reduce out-of-plane bending of the shuttle [3]. Another method of decreasing heating of the shuttle is to utilize a cascaded actuator structure [4,26,27]. Cascaded structures are typically used to multiply the displacement output of a given actuator design. Abbas et al. shows that the maximum temperature of the shuttle of in a cascaded design is be 22 °C with a global maximum operating temperature of 315 °C. A similar design using heat sinks show a maximum shuttle temperature of 148 °C for a global maximum operating temperature of 500 °C [4].

Finally, to prevent the growth of an oxide layer from forming on the actuator during high temperature/ high displacement operation, as was seen by Baker et al [30] , an atomically thin coating of hexagonal boron nitride (h-BN) could be deposited onto the actuator. Liu et al. recently demonstrated that by coating copper, steel, or nickel foil with h-BN that the materials could withstand oxidizing at temperatures up to 1,100 °C [59].

After fabricating and characterizing an improved design of the thermally actuated fiber based Fabry-Pérot MEMS interferometer, the next step would be to integrate the improved design into an application such as a nanomaterial tester, as feedback for closed loop control of a positioning system, or as a tunable micro cavity for use in QED experiments.

## **7.4 Concluding Remarks**

As shown in the results from both experiments, while the concept of the device has been proven, modifications to the overall device need to be made before it could be used in various applications due to the heating of the shuttle. Potential improvements to the device have been suggested. The next chapter summarizes the key points of this document to conclude the thesis.

## Chapter 8: Conclusion

Once again, the objective of this thesis was to present a thermally actuated fiber based Fabry-Pérot device that, with some improvements, has the potential be integrated into more complex devices such as a nanomaterial characterization system or as a tunable atom/ion trap for use in micro QED experiments.

Background of the theory of both thermal actuators and Fabry-Pérot cavities was given to aid in understanding the design choices made in designing the device as well as the methods used in modeling the thermal actuators and the Fabry-Pérot cavities. The importance of using temperature dependent materials in any simulation, FEA based or analytically derived, was also highlighted in chapter 2.

The design of the device was presented to highlight the overall design of the thermally actuated fiber based Fabry-Pérot interferometric MEMS device. Chapter 3 highlights unique design features of the device such as the alignment trench that is etched into in the thermal actuator used to aid in placing the fiber mirrors onto the thermal actuator structure. Parameters that affect the performance of thermal actuator of the Fabry-Pérot cavity were also mentioned in this chapter. Methods used to fabricate the thermal actuator, the device holder used to mount and transport the device between test setups, and the fabrication and placement of the fiber mirrors have been presented in chapter 4.

Chapter 5 showed how a thermal actuator was characterized in a vacuum environment inside of an SEM and in air with the cavity attached. Experiments in SEM confirmed that heating and expansion of the shuttle is not negligible and can affect the measured displacement. Displacement data was gathered using image analysis in the SEM



experiments, and extrapolated from data obtained from the Fabry-Pérot cavity taken during the in air experiments.

Details of the modeling performed were also outlined in chapter 6. A multiphysics FEA model utilizes temperature dependent material properties. A MATLAB model of the Fabry-Pérot cavity was created to determine the change in length of the cavity while the thermal actuator operated in air.

Results of displacement versus current data were compared to the modeling in chapter 7. Displacement obtained from the multiphysics FEA model matched well with the displacement data obtained from the experiments performed in SEM. Displacement data obtained from the Fabry-Pérot cavity during the in air tests show that there are improvements to be made on this device before it can be used in an application. Suggestions of improvements that could be made to the design of the device and of the experiment were presented at the end of chapter 7.

## Appendix 1: Derivation of the Cavity Length Formula Used in the Two-Fringe Method

For a FP cavity, the total phase difference between two successive beams, as shown in Figure 9 in chapter 2, is as follows.

$$\Delta = \delta + \delta_r$$

In the above expression,  $\delta$  is the phase difference between any two successive rays as given by the following equation.

$$\delta = \frac{4\pi}{\lambda_o} n \cdot d_{cav} \cdot \cos\phi$$

In the above equation,  $n$  is the index of refraction of the medium between the cavity mirrors,  $\lambda_o$  is the vacuum wavelength of the laser,  $d_{cav}$  is the cavity length, and  $\phi$  is the angle between any two successive rays.  $\delta_r$  is the phase change for one round trip of a beam due to reflection.

In order to have a fringe minimum, the following condition must be satisfied in which the total phase change is  $\Delta = 2N\pi$  where  $N$  is any integer. Applying this condition to the equation above we obtain the following expression.

$$2N\pi = \frac{4\pi}{\lambda_o} n \cdot d_{cav} \cdot \cos\phi + \delta_r$$

In this experiment, air is the medium between the mirrors so  $n=1$  and we assume that  $\phi$  approaches zero so that equation above may be simplified down to the following expression.

$$2N\pi = \frac{4\pi}{\lambda_o} d_{cav} + \delta_r$$

To find the cavity length, one can use any two adjacent fringe minima, as shown in Figure 10 in chapter 2. The fringes can be represented by the following equations where  $2N\pi$  is one fringe and  $2(N+1)\pi$  is the adjacent fringe.

$$2N\pi = \frac{4\pi}{\lambda_1}d_{cav} + \delta_r$$

$$2(N+1)\pi = \frac{4\pi}{\lambda_2}d_{cav} + \delta_r$$

Setting both of the above equations equal to N we obtain the following expressions.

$$N = \frac{1}{2\pi} \left( \frac{4\pi d_{cav}}{\lambda_1} + \delta_r \right)$$

$$N = \frac{1}{2\pi} \left( \frac{4\pi d_{cav}}{\lambda_2} + \delta_r \right) - 1$$

Setting equation the above equations equal to each other and simplifying we can obtain the cavity length,  $d_{cav}$  as shown in the following steps.

$$\frac{4\pi d_{cav}}{\lambda_1} = \frac{4\pi d_{cav}}{\lambda_2} - 2\pi$$

$$\frac{4\pi d_{cav}}{\lambda_1} = 2\pi \left( \frac{2d_{cav}}{\lambda_2} - 1 \right)$$

$$1 = \frac{2d_{cav}}{\lambda_2} - \frac{2d_{cav}}{\lambda_1}$$

$$1 = 2d_{cav} \frac{(\lambda_1 - \lambda_2)}{\lambda_2 \lambda_1}$$

$$d_{cav} = \frac{\lambda_2 \lambda_1}{2(\lambda_2 - \lambda_1)}$$

## Appendix 2: Definition of Variables

$\alpha_{act}$  - Coefficient of thermal expansion of the actuator material.

$\alpha_{si}$  - Coefficient of thermal expansion of single crystalline silicon.

$\beta$  - Temperature coefficient of resistance.

$\gamma$  - Relative magnitude of internal heat flux to the heat flux out to the surroundings.

$\Delta$  - Combined phase difference between two adjacent beams and from reflection.

$\Delta L$  - Change in actuator arm length due to thermal expansion.

$\Delta T$  - Average temperature of actuator arm (see  $T_{ave}$ ).

$\Delta T_{wall}$  - Temperature difference between two sides of a wall.

$\Delta z$  - Distance from the top surface of the substrate to the bottom surface of the actuator.

$\delta$  - Phase change between two adjacent beams of light.

$\delta_r$  - Phase change of a beam of light due to reflection.

$\varepsilon_{act}$  - Emissivity of actuator material.

$\theta$  - Initial bias angle of actuator arms.

$\lambda$  - Wavelength of light.

$\lambda_1$  - Wavelength of the center of a fringe from a graph of the airy function.

$\lambda_2$  - Wavelength of the center of a fringe adjacent to  $\lambda_1$ .

$\xi$  - Stiffness term used by Que et al. and Enikov et al. (see chapter 2).

$\rho_{act}$  - Resistivity of actuator material.

$\rho_o$  - Resistivity of a material at room temperature.

$\rho_{si}$  - Resistivity of single crystalline silicon.

$\sigma$  - Stefan-Boltzmann constant.

$\phi$  - Angle between two adjacent light rays.

$\psi$  - Constant used by Zhu et al. (see chapter 2).

$\omega$  - Parameter of heat conduction of air vs. heat conduction of actuator material.

$A$  - Absorptivity of mirror.

$A_{b_i}$  - Area of the bottom side of the actuator arm.

$A_{s_i}$  - Total surface area of the actuator arm.

$A_{wall}$  - Cross sectional area of a wall.

$A_x$  - Cross sectional area of an actuator arm.

$d$  - Displacement of an actuator shuttle.

$d_o$  - Initial projected height of an actuator arm.

$d_{cav}$  - Cavity length of Fabry-Pérot cavity.

$d_{cav_i}$  - Length of Fabry-Pérot cavity at a given current applied to the TA.

$E$  - Young's modulus.

$E_a$  - Fitting parameter in KOH etch model.

$E_o$  - Initial amplitude of the electric field associated with light rays.

$E_T$  - Amplitude of the transmitted electric field associated with light rays.

$E_R$  - Amplitude of the reflected electric field associated with light rays.

$F$  - Coefficient of finesse.

$\vec{F}_a$  - Force along axis of the actuator arm.

$\vec{F}_x$  - Force imparted to actuator arm.

G. A. – Geometric Amplification.

$I$  - Area moment of inertia.

$I_{est}$  - Amplitude of airy function estimated from data.

$I_{fit}$  - Airy function fitted to data.

$I_o$  - Initial Intensity of light entering a Fabry-Pérot cavity.

$I_R$  - Airy function of reflected light from a Fabry-Pérot cavity.

$I_T$  - Airy function of transmitted light from a Fabry-Pérot cavity.

$i$  - Current applied to actuator.

$j$  - Imaginary number.

$K_{act}$  - Thermal conductivity of the actuator material.

$K_{air}$  - Thermal conductivity of air.

$k_b$  - Boltzmann constant.

$K_{eff}$  - Effective thermal conductivity of a stack of materials.

$k_o$  - Fitting parameter in KOH etch model.

$K_{si}$  - Thermal conductivity of single crystalline silicon.

$L$  - Initial length of actuator arm from bond pad to shuttle.

$L_i$  - Length of a volume element of an actuator arm.

$L_p$  - Projected length of an actuator arm.

$L_{wall}$  - Thickness of a wall.

$\vec{M}_R$  - Moment imposed on actuator arm.

$N$  - Any integer value.

$n$  - Index of refraction of material between mirrors of Fabry-Pérot cavity.

$P_{b_i}$  - Perimeter of the bottom of a actuator arm.

$q_{air}$  - Heat flux to the air.

$q_{gen}$  - Heat flux generated by Joule heating.  
 $q_{i\pm 1}$  - Heat flux to/from adjacent volume elements.  
 $q_{rad}$  - Heat flux via radiation.  
 $q_{wall}$  - Heat flux through a wall.  
 $R$  - Total reflectivity of a Fabry-Pérot cavity.  
 $R_1$  - Reflectivity of one mirror of a Fabry-Pérot cavity.  
 $R_2$  - Reflectivity of one mirror of a Fabry-Pérot cavity.  
 $R_{etch}$  - Etch rate of single crystal silicon in KOH.  
 $R_{act}$  - Resistance of actuator material.  
 $S$  - Conduction Shape Factor.  
 $T$  - Total transmissivity of a Fabry-Pérot cavity.  
 $T_1$  - Transmissivity of one mirror of a Fabry-Pérot cavity.  
 $T_2$  - Transmissivity of one mirror of a Fabry-Pérot cavity.  
 $T_{ave}$  - Average temperature of an actuator arm (see  $\Delta T$ ).  
 $T_i$  - Temperature of a volume element.  
 $T_{i\pm 1}$  - Temperature of adjacent volume elements.  
 $T_{sub}$  - Temperature of the substrate.  
 $t$  - Thickness of an actuator arm as defined by the thickness of the device layer.  
 $V$  - Voltage.  
 $\forall_i$  - Volume of a volume element.  
 $w$  - Width of an actuator arm.  
 $x$  - Distance along an axis running parallel to the actuator arm.

## References

- [1] Feynman R P 1960 There's plenty of room at the bottom *Eng. Sci.* **23** 22–36
- [2] Marsh D M 1961 Micro-tensile testing machine *J. Sci. Instrum.* **38** 229–34
- [3] Zhu Y, Corigliano A and Espinosa H 2006 A thermal actuator for nanoscale in situ microscopy testing: design and characterization *J. Micromechanics* **16** 242–53
- [4] Abbas K, Alaie S and Leseman Z C 2012 Design and characterization of a low temperature gradient and large displacement thermal actuators for in situ mechanical testing of nanoscale materials *J. Micromechanics Microengineering* **22**
- [5] Lin C-J and Tseng F-G 2004 A micro Fabry–Perot sensor for nano-lateral displacement sensing with enhanced sensitivity and pressure resistance *Sensors Actuators A Phys.* **114** 163–70
- [6] Unamuno a., Yao J and Uttamchandani D 2005 Alignment and fixing of fiber optics based on electrothermal MEMS actuators *IEEE Photonics Technol. Lett.* **17** 816–8
- [7] Kim Y-S, Dagalakis N G and Gupta S K 2013 Creating large out-of-plane displacement electrothermal motion stage by incorporating beams with step features *J. Micromechanics Microengineering* **23**
- [8] Banerjee A S, Blaikie R and Wang W H 2011 Microfabrication Process for XYZ Stage-Needle Assembly for Cellular Delivery and Surgery *Mater. Sci. Forum* **700** 195–8
- [9] Sahu B, Taylor C R and Leang K K 2010 Emerging Challenges of Microactuators for Nanoscale Positioning, Assembly, and Manipulation *J. Manuf. Sci. Eng.* **132**
- [10] Kim C and Jeong H 2003 Silicon micro XY-stage with a large area shuttle and notching holes for SPM-based data storage *J. Microelectromechanical Syst.* **12** 470–8
- [11] Choi Y-S, Zhang Y and Lee D-W 2012 A thermal-driven silicon micro xy -stage integrated with piezoresistive sensors for nano-positioning *J. Micromechanics Microengineering* **22**
- [12] Lin C-Y and Chiou J-C 2012 Design and fabrication of MEMS-based thermally-actuated image stabilizer for cell phone camera *Solid. State. Electron.* **77** 64–71
- [13] Hunger D, Steinmetz T, Colombe Y, Deutsch C, Hänsch T W and Reichel J 2010 A fiber Fabry–Perot cavity with high finesse *New J. Phys.* **12**



- [14] Steinmetz T, Colombe Y, Hunger D, Hänsch T W, Balocchi A, Warburton R J and Reichel J 2006 Stable fiber-based Fabry-Pérot cavity *Appl. Phys. Lett.* **89**
- [15] Hunger D and Steinmetz T 2010 A fiber Fabry-Perot cavity with high finesse *New J. Phys.* **12**
- [16] Reiserer A, Ritter S and Rempe G 2013 Nondestructive Detection of an Optical Photon *Science.* **342**
- [17] Derntl C, Schneider M, Schalko J, Bittner A, Schmiedmayer J, Schmid U and Trupke M 2013 Arrays of open, independently tunable microcavities *ArXiv* 7
- [18] Hendrickson S M, Weiler C N, Camacho R M, Rakich P T, Young A I, Shaw M J, Pittman T B, Franson J D and Jacobs B C 2013 All-optical-switching demonstration using two-photon absorption and the Zeno effect *Phys. Rev. A* **87**
- [19] Hendrickson S, Weiler C, Camacho R M, Rakich P T, Young A I, Shaw M J, Franson J and Jacobs B 2011 Observation of low-contrast all-optical switching based on the Zeno effect *Front. ...* **1** 2–3
- [20] Timoshenko 1925 Analysis of bi-metal thermostats *J. Opt. Soc. Am*
- [21] Chu W, Mehregany M and Mullen R 1993 Analysis of tip deflection and force of a bimetallic cantilever microactuator *J. Micromechanics Microengineering* **4** 3–7
- [22] Liu K, Cheng C, Cheng Z, Wang K, Ramesh R and Wu J 2012 Giant-amplitude, high-work density microactuators with phase transition activated nanolayer bimorphs. *Nano Lett.* **12**
- [23] Huang Q-A and Lee N K S 1999 Analysis and design of polysilicon thermal flexure actuator *J. Micromechanics Microengineering* **9** 64–70
- [24] Syms R R A 2002 Long-travel electrothermally driven resonant cantilever microactuators *J. Micromechanics Microengineering* **12** 211–8
- [25] Que L, Otradovec L, Oliver A D and Gianchandani Y B 2001 Pulse and DC operation lifetimes of bent-beam electrothermal actuators *Technical Digest. MEMS 2001. 14th IEEE International Conference on Micro Electro Mechanical Systems (Cat. No.01CH37090)* (IEEE) pp 570–3
- [26] Gianchandani Y B 2001 Bent-beam electrothermal actuators-Part I: Single beam and cascaded devices *J. Microelectromechanical Syst.* **10** 247–54
- [27] Howell L, McLain T W, Baker M S and Lott C D 2006 *MEMS/NEMS Handbook, Techniques and Applications. Chapter 7: Techniques in the Design of Thermomechanical Microactuators* ed C T Leondes (Boston, MA: Springer US)

- [28] Lott C D, McLain T W, Harb J N and Howell L L 2002 Modeling the thermal behavior of a surface-micromachined linear-displacement thermomechanical microactuator *Sensors Actuators A Phys.* **101** 239–50
- [29] Girbau D, Roldan A and Pradell L 2003 RF MEMS switches based on the buckle-beam thermal actuator *Microw. Conf. 2003* 3–6
- [30] Baker M, Walraven J, Headley T and Plass R 2004 *Final Report: Compliant Thermo-mechanical MEMS Actuators, LDRD# 52553* (Albuquerque)
- [31] Matmat M, Ahmad M A L and Fourniols J Y 2007 Perspectives of Thermo-electro-mechanical Micro actuators for micro switch Applications : Design and Simulation *COMSOL Users Conference 2007* (Gernoble)
- [32] Hickey R, Sameoto D, Hubbard T and Kujath M 2003 Time and frequency response of two-arm micromachined thermal actuators *J. Micromechanics Microengineering* **13** 40–6
- [33] Kushkiev I and Jupina M A 2005 Modeling the Thermo-Mechanical Behavior of a “ V ” -Shaped Composite Buckle-Beam Thermal Actuator II . Numerical Model of the Pre-Bent Beam *COMSOL Users Conference 2005* (Boston, MA)
- [34] Enikov E T, Kedar S S and Lazarov K V 2005 Analytical model for analysis and design of V-shaped thermal microactuators *J. Microelectromechanical Syst.* **14** 788–98
- [35] Lai Y, McDonald J, Kujath M and Hubbard T 2004 Force, deflection and power measurements of toggled microthermal actuators *J. Micromechanics Microengineering* **14** 49–56
- [36] Çengel Y A and Ghajar A J 2011 *Heat and Mass Transfer: Fundamentals & Applications* (McGraw-Hill Companies)
- [37] Lin L and Chiao M 1996 Electrothermal responses of lineshape microstructures *Sensors Actuators A Phys.* **55** 35–41
- [38] Tolansky S 1973 *An Introduction to Interferometry* (London: Longman)
- [39] Wang T, Zheng S and Yang Z 1998 A high precision displacement sensor using a low-finesse fiber-optic Fabry-Perot interferometer *Sensors Actuators A Phys.* **69** 134–8
- [40] Santos J L, Leite a P and Jackson D a 1992 Optical fiber sensing with a low-finesse Fabry-Perot cavity. *Appl. Opt.* **31** 7361–6

- [41] Qi B, Pickrell G R, Xu J, Zhang P, Duan Y, Peng W, Huang Z, Huo W, Xiao H, May R G and Wang A 2003 Novel data processing techniques for dispersive white light interferometer *Opt. Eng.* **42** 3165
- [42] Seat H C and Pullteap S 2007 An Extrinsic Fiber Fabry-Perot Interferometer for Dynamic Displacement Measurement *2007 International Conference on Mechatronics and Automation (Ieee)*
- [43] Fowles G R 1989 *Introduction to Modern Optics* (New York: Dover Publications)
- [44] Hecht E 2002 *Optics* (Addison-Wesley Longman, Incorporated)
- [45] Holden J 1949 Multiple-beam interferometry: intensity distribution in the reflected system *Proc. Phys. Soc. Sect. B* **405**
- [46] Tolansky S 1946 The intensity efficiency of the Fabry-Pérot interferometer. Both in transmission and reflection. *Physica* **12** 649–55
- [47] Macleod H A 2001 *Thin-Film Optical Filters* (CRC Press)
- [48] Palik E 1998 *Handbook of Optical Constants of Solids* ed E Palik (Academic Press)
- [49] Weber E M J, Dotsenko A V, Glebov L B and Tsekhomsky V A 2003 *Handbook of Optical Materials* (CRC Press)
- [50] Vangbo M and Bäcklund Y 1996 Precise mask alignment to the crystallographic orientation of silicon wafers using wet anisotropic etching *J. Micromechanics Microengineering* **6** 279–84
- [51] Seidel H and Csepregi L 1990 Anisotropic etching of crystalline silicon in alkaline solutions *J. Electrochem. Soc.* **137** 249–60
- [52] Williams K and Muller R 1996 Etch rates for micromachining processing *J. Microelectromechanical Syst.* **5**
- [53] Gad-el-Hak M 2010 *MEMS: Design and Fabrication* (New York: CRC Press)
- [54] Harman G G 1997 *Wire Bonding in Microelectronics: Materials, Processes, Reliability, and Yield* (McGraw-Hill)
- [55] Okada Y and Tokumaru Y 1984 Precise determination of lattice parameter and thermal expansion coefficient of silicon between 300 and 1500 K *J. Appl. Phys.* **56** 314

- [56] Hull R 1999 *Properties of crystalline silicon* (The Institution of Electrical Engineers (INSPEC))
- [57] Torczynski J R, Gallis M A, Piekos E S, Serrano J R, Phinney L M and Gorby A D 2008 *Validation of Thermal Models for a Prototypical MEMS Thermal Actuator* (Albuquerque)
- [58] Various 2004 *Optimization Toolbox for Use with MATLAB: User's Guide, Version 3* (Natick, MA: MathWorks)
- [59] Liu Z, Gong Y, Zhou W, Ma L, Yu J, Idrobo J C, Jung J, Macdonald A H, Vajtai R, Lou J and Ajayan P M 2013 Ultrathin high-temperature oxidation-resistant coatings of hexagonal boron nitride. *Nat. Commun.* **4** 2541